

Diese Arbeit hat beurteilt:

Univ. Prof. Reinhard Pippan



TECHNISCHE
UNIVERSITÄT
WIEN

Vienna University of Technology

DIPLOMARBEIT

The influence of Hydrogen and Nitrogen impurities on the annealing behaviour of undoped silicon glass

Ausgeführt am Institut für

Festkörperphysik

der Technischen Universität Wien

in Zusammenarbeit mit dem

Erich Schmid Institut für Materialwissenschaften

unter der Anleitung von

Prof. Dr. Reinhard Pippan, Dr. Megan Cordill

durch

Stephan Paul Biegl

Name

Wienerbergstraße 16-20 1312, 120 Wien

Anschrift

28.08.2013

Datum

Stephan P. Biegl

Unterschrift (Student)

Abstract

In today's semiconductor industry materials and deposition techniques have to fulfill the sophisticated product requirements of modern microelectronic devices. To meet the quality standards of the desired products thin film deposition process have to be tuned very accurately to any avoid contaminations and incorporations of chemical impurities.

For that reason a wafer curvature instrument was developed enabling the characterization of the thermomechanical behavior of semiconductor materials from room temperature up to 1000°C. This allowed the investigation of the stress evolution of nitrogen and hydrogen doped undoped silicon glass (USG) SiO_2 films during an annealing process which are performed at the same temperatures as industrial deposition. Based on the stress-temperature results and complementary characterization techniques of infrared spectroscopy, nanoindentation, ellipsometry, light microscopy and atomic force microscopy a qualitative model was developed to describe the influence of nitrogen and hydrogen in terms of the stress evolution and resulting crack formation.

Films A, B, C and D were USG films deposited via PECVD process with a standardized thickness of 1000 nm. Films B, C and D represent an improved SiO_2 film (B), a production silane based USG (C), and a production TEOS based USG film (D). All of the films have a qualitative film composition of about SiO_xH_y . Using higher silane gas flow and additional ammonia gas flow, Film A resulted in $\text{SiO}_x\text{N}_y\text{H}_z$ film composition. During a thermal cycle nitrogen and hydrogen impurities caused massive tensile stress generation to occur at 550°C leading to maximum tensile stresses of about 1GPa at 1000°C. Crack formation occurred between 700°C and 800°C due to a tensile stress between 430 MPa and 780°C. After one thermal cycle the elastic modulus of Film A increased 38% up to 97 GPa, while the film thickness decreased 11%. The investigation led to the qualitative model where remaining trapped nitrogen and hydrogen species are released beginning at 550°C due the build-up of thermal stresses. Further stress increase is caused by hydrogen bond cleavage from Si-H and N-H species starting around 700°C. Intrinsic stresses are generated by following cross linking reactions between silicon and nitrogen species which leads to massive tensile stresses that result in film cracking after exceeding a critical film stress. The qualitative composition of Film A after one thermal cycle became SiO_xN_y indicating a silicon oxynitride film with almost no remaining hydrogen. The hydrogen species was the origin of large tensile stress generation and nitrogen species was the dopant agent leading to mechanically harder and stiffer films where the cross linking reactions induce compressive stresses due to the different binding nature between nitrogen and silicon atoms compared to oxygen atoms in USG.

Kurzfassung

In der heutigen Halbleiter Industrie müssen sowohl Materialien als auch die dazugehörigen Abscheidungsprozesse die hohen Produkthanforderungen der mikroelektronischen Bauteile erfüllen. Um diese Qualitätsstandards der einzelnen Produkte zu erreichen müssen die angewandten Dünnschicht-Abscheidungsverfahren sehr genau abgestimmt werden um jegliche Kontaminationen und Einlagerung von chemischen Verunreinigungen zu vermeiden.

Aus diesem Grund wurde eine Substrat-Krümmungs Messanlage aufgebaut, mit der es möglich ist das thermomechanische Verhalten von Halbleiter Materialien von Raumtemperatur bis 1000°C zu beobachten. Dies ermöglicht Untersuchungen der Spannungsevolution von mit Stickstoff und Wasserstoff dotierten USG (undodiertes Silizium Glas, SiO_2) Schichten während einer Wärmebehandlung, welche in etwa jenem Temperaturbereich der industriellen Abscheidung entspricht. Basierend auf den erhaltenen Spannungs- Temperatur Messergebnissen und den komplementär genutzten Charakterisierungsmethoden wie Infrarotspektroskopie, Nanoindentation, Ellipsometrie, Lichtmikroskopie und Atomkraftmikroskopie (AFM), wurde ein qualitatives Model entwickelt, welches den Einfluss von Stickstoff und Wasserstoff in Bezug auf die Spannungsevolution und die daraus resultierende Rissbildung zeigt.

Schichten A, B, C und D sind USG Schichten, welche durch einen PE-CVD Prozess mit standardisierten Schichtdicken von 1000 nm abgeschieden worden sind. Filme B, C und D repräsentieren dabei jeweils: eine verbesserte SiO_2 Schicht (B), eine produktive auf Silane basierende Schicht (C) und eine produktive auf TEOS basierende USG Schicht (D), wobei (D) eine qualitativen Schichtzusammensetzung von SiO_xH_y besitzt, welche als Referenzmaterial verwendet wird. Durch einen höheren Silan Gasfluss und einen zusätzlichen Ammoniak Gasfluss, resultierte die chemische Zusammensetzung in $\text{SiO}_x\text{N}_y\text{H}_z$ für die Schicht A. Während eines thermischen Zyklus führten N und H Verunreinigungen zur Generierung zusätzlicher Zugspannungen, welche bei etwa 550°C das erste Mal auftreten und bis zu maximalen Zugspannungen im Bereich von etwa 1 GPa bei 1000°C führten. Die hierbei beobachtete Rissbildung tritt zwischen 700°C und 800°C ein, wobei die Bruchspannung für die Rissbildung zwischen 430 MPa und 780 MPa liegt. Nach einem thermischen Zyklus stieg der elastische Modul um 38% auf 97 GPa an, wobei sich die Filmdicke um etwa 11% reduzierte. Diese Untersuchungen führen zu einem qualitativen Modell wo die gebundenen Stickstoff und Wasserstoff Verunreinigungen zu massiven zusätzlichen Zugspannungen führen, welche bei etwa 550°C erstmals auftreten, gleichzeitig mit der beginnenden Ausgasungen von eingebauten Gasmolekülen. Der weitere Spannungsanstieg erfolgt durch die Abspaltung von Wasserstoff von Si-H und N-H Molekülen, beginnend bei ungefähr 700°C. Die weiteren intrinsischen Spannungen werden durch darauffolgende Quervernetzungsreaktionen zwischen Silizium und Stickstoff Atomen erzeugt, welche zu starken

Zugspannungen und einer anschließende Rissbildung führen nach dem eine kritische Schichtspannung überschritten wird. Die qualitative Zusammensetzung nach einer thermischen Belastung von Schicht A wurde als SiO_xN_y identifiziert, mit beinahe keinem verbleibenden Wasserstoff in der Schicht. Der Wasserstoff wurde als ausschlaggebende Ursache für die große Zugspannungsentwicklung identifiziert. Die Stickstoff Atome als Dotierungsreagenzien führten zu einer mechanischen härteren und steiferen Schicht, wobei Quervernetzungsreaktionen als Druckspannungsinduzierende Reaktionen beschrieben werden, aufgrund der unterschiedlichen Bindungsnatur zwischen Stickstoff und Silizium Atomen verglichen mit Sauerstoff Atomen in USG.

Table of Contents

Table of figures.....	V
Table of tables.....	VII
Introduction	1
1.1 Motivation.....	1
1.2. Undoped Silicon Glass in the Microelectronic Industry	2
1.3. Fundamentals of SiO ₂	4
1.4. Deposition process of amorphous Silicon dioxide.....	6
1.5. Mechanical Stresses in amorphous thin Film processing	10
1.6. Wafer Curvature Method	13
1.7. Fourier Transform-Infrared Spectroscopy	16
1.8. Nanoindentation	18
2. Experimental and deposition results.....	20
2.1. Film deposition and characterisation.....	20
2.2. Sample preparation	22
2.3. FT-IR as-deposited results	23
2.4. Surface Analysis	26
2.5. Mechanical properties of the as-deposited films	28
3. Thermal Cycling to 1000°C	31
3.1. Wafer Curvature Experiments.....	31
3.2. FT-IR.....	36
3.3. Surface Characterisation	38
3.4. Nanoindentation	39
4. Temperature resolved experiments of Film A.....	41
Differentiation of Nitrogen and Hydrogen Influence.....	48
5. Discussion	51
6. Summary and Future Work	61
Bibliography	64

Table of figures

Figure 1: Micro machined MEMS device for optoelectronic applications where USG films are used as mechanical supporting layers for Si ₃ N ₄ and Germanium [4].	3
Figure 2: Structural properties of SiO ₂ which displays the tetrahedral SiO ₄ unit (a), the bond arrangement and the corresponding angles between silicon and oxygen (b) and a schematic structure model of glass(c) [7].	5
Figure 3: Schematic process chamber of the PECVD silane deposition. Silicon substrate is heated via a ceramic heater plate. Additional energy is supplied via RF-plasma which activates the incoming gas stream.	7
Figure 4: Basic transport scheme of reactant gases to the substrate surface.	8
Figure 5: Schematic illustration of a thin film deposited on a substrate which can result in tensile or compressive film stresses.	10
Figure 6: Stress analysis of thin films. (a) displays the thin film/substrate composite. (b) shows indicates the interfacial forces and moments of the film and the substrate displayed as simple plates, (c)	12
Figure 7: Schematic illustration of the used KSA multi-beam optical sensor (MOS). A laser beam array is generated via optical devices, which is reflected by the sample and detected using a charge coupled device (CCD) detector [22].	13
Figure 8: Basic relationship between the sample curvature and the measured beam deflection [21].	14
Figure 9: Typical Stress-temperature data of a polycrystalline aluminium film deposited on a silicon substrate. The thermocycle indicates linear compressive stress generation due to CTE mismatch and following relaxation events in aluminium [23].	15
Figure 10: Basic scheme of FT-IR processing. The sample is exposed to a beam of light in an interferometer which creates a specific interferogram. Via a Fourier transformation a spectrum is obtained where the signal is a function of the wave number.	16
Figure 11: FT-IR absorption spectrum of a silane based USG film. The vibration modes displayed on the graph indicate the motion of the oxygen atom in the stretching, bending and rocking vibration modes with the corresponding energies for a stoichiometric SiO ₂ film compared to the three labelled wave numbers from a PECVD deposited USG film.	17
Figure 12: Load-displacement curve indicating the determination of the stiffness in the unloading curve [29].	19
Figure 13: Affected volume during indentation mode in a thin film sample [30].	19
Figure 14: Back side of a coated 200 mm silicon wafer indicating the cutting lines.	22
Figure 15: Infrared spectra of Films A, B, C and D. Film A reveals additional peaks due to nitrogen and hydrogen doping, whereas the other three films only exhibit minor impurities of silanol (Si-OH) groups.	24
Figure 16: Comparison of the IR spectra between the nitrogen and hydrogen-rich USG film, Film A and the production USG film, Film C.	25
Figure 17: Light microscope images of Films A, B and C and D after deposition, indicating the crack-free surfaces.	26
Figure 18: AFM 3-D height image of Film C showing representative surface roughness of amorphous silicon dioxide.	27

Figure 19: Elastic moduli of Films A, B, C and D after deposition. All films exhibit a linear behaviour with contact depth. Films B, C and D have similar elastic properties, while Film A has a lower elastic modulus.....	29
Figure 20: Wafer curvature system for high temperature measurements. Left image shows the setup of the measurement device. Right image displays the heating plate and the built-in thermo-element for temperature control.	32
Figure 21: Stress-Temperature cycles of Films A, B, C and D. The thermomechanical behaviour of Films A, B and C can be described as completely thermoelastic, in contrast to Film B which shows large irreversible stress changes due to hydrogen and nitrogen species.	34
Figure 22: Comparison between Film A (high Nitrogen + Hydrogen content) and Film B (optimised USG film) wafer curvature curves. Massive stress evolution starting around 550°C in Film A can be observed.....	35
Figure 23: FT-IR spectra of Films A, B, C and D after one thermal cycle. Disappearance of Si-H and Si-N-H band and peak reduction around 900-700 cm ⁻¹ in Film A. Spectra of Films B, C and D remain more or less unchanged after heat treatment, except for the disappearance of the small Si-OH band	36
Figure 24: Optical image of Film A illustrating the parallel crack arrays found after thermal cycling.....	38
Figure 25: Comparison of the elastic moduli before and after a complete thermal cycle of Films A, B, C and D. Films B, C and D remain approximately unchanged in terms of their elastic properties, whereas Film A shows a large increase due to chemical changes indicated by the FT-IR data.....	39
Figure 26: Wafer curvature heat cycles with different peak temperatures. Up to 500°C no irreversible stress generation can be observed. Higher peak temperatures lead to large stress changes.....	42
Figure 27: Chemical evolution of Film A with different peak temperatures. Bond cleaves of Hydrogen occurs between temperatures of 700°C and 1000°C.	43
Figure 28: Thermally resolved elastic properties of Film A which display a large increase of the elastic modulus starting around 550°C.....	44
Figure 29: Thermal resolved hardness data of Film A, which displays a large increase at temperatures greater than 550°C.....	45
Figure 30: Thermal resolved film thickness of Film A. At peak temperatures between 500°C and 600°C the film thickness starts to decrease which results in a thickness loss of about 11% after one thermal cycle.	46
Figure 31: Thermal resolved optical properties of Film A. The refractive index increases significantly with temperatures greater than 800°C.....	47
Figure 32: Stress evolution of an high N film (Film E) and a high H film (Film F) compared to Film A with a high N and H concentration	49
Figure 33: Light microscopy images of Film A and F. Film F revealed only a few cracks which were thin compared to Film A.	49
Figure 34: Structural 2-D model of Film A containing high nitrogen and hydrogen impurities after deposition.....	54
Figure 35: One of the four sp ³ hybrid orbitals of a silicon atom. Each one points towards a different vertex (green line) resulting in a regular tetrahedra [44].....	55

Figure 36: Film thickness shrinkage due to release of trapped molecular species in Film A.....56

Figure 37: Three possible hydrogen removal reactions and following crosslinking between the remaining species. (a) reaction between a silane group (Si-H) and a Silanol group (Si-OH), (b) reaction between two Silane groups and (c) hydrogen removal via a Si-H and N-H group.....57

Figure 38: Structural model after heat treatment. The distorted structure indicates the generated tensile stresses due to hydrogen bond cleavage and following cross linking. The dots near silicon and nitrogen atoms indicate electronic defects in the glass network.....58

Table of tables

Table 1: Properties of USG as bulk material [7]4

Table 2: Deposition parameters of Films A, B, C and D 20

Table 3: Initial film properties which were obtained at the plant side.....21

Table 4: RMS roughness and absolute height values of Film A, B, C in the as deposited state.28

Table 5: As deposited mechanical data of Films A, B, C and D. 29

Table 6: Summary of the wafer curvature results of Films A, B, C and D..... 35

Table 7: RMS roughness and absolute height values of Film A, B, C and D after one thermal cycle. 38

Table 8: Summary of the mechanical properties of the as deposited and after one thermocycle of Films, A, B, C and D. 40

Table 9: Thermally resolved stress-temperature data of Film A.....42

Table 10: Deposition parameters and initial properties of Film E and F compared to the high N and H containing Film A.....48

Table 11: Stress-Temperature Data of Films A, E and F. 50

Introduction

1.1 Motivation

Undoped silicon glass (USG), which is chemically assigned as silicon dioxide (SiO_2), is the most common dielectric material in the microelectronics industry. Due to its excellent thermal and electrically insulating properties, its relatively low manufacturing cost, and the variety of deposition processes, it's relatively low manufacturing cost, and the variety of deposition processes, it has been used over the past decades as a standard dielectric layer. This amorphous material has been used as dielectric gate material, inter-level dielectric layer, insulating and passivation layers, and as well of its chemical and mechanical stability[1].

During the deposition of USG, which vary in thickness from a few nanometers (nm) up to several microns (μm), the films are exposed to annealing temperatures up to 1050°C . Due to nitrogen and hydrogen impurities left over from the deposition conditions of the plasma enhanced-chemical vapour deposition (PE-CVD) the device can mechanically fail. The impurities can cause a structural and chemical change at higher temperatures leading to additional tensile stresses which then results in fracture of the brittle film material. The cracked film makes the electronic micro device unusable.

To get a deeper understanding of the stress behaviour of USG films during the heat treatment, a wafer curvature system was constructed that allows the observation of the thermomechanical stress evolution from room temperature up to 1000°C . This can show in-situ stress changes due to temperature and chemical changes. To develop a fundamental model of the stress evolution due to nitrogen and hydrogen impurities additional characterisation techniques such as nanoindentation and Fourier transform-infrared spectroscopy (FT-IR) were used.

1.2. Undoped Silicon Glass in the Microelectronic Industry

Since the invention of the bipolar transistor in 1947, the microelectronics industry continues its imposing triumph in today's modern electronics world. To understand why the quality of such dielectric amorphous films like silicon dioxide (SiO_2) is so important, a brief overview of the field of applications will show its significance.

During the rapid growth of the semiconductor-industry during the 50s and 60s microelectronic devices have become significantly smaller. Therefore, a new subtype of device, Micro-Electro-Mechanical Systems (MEMS) has been developed to continue the race of miniaturisation and efficiency-gain. This technology, in its most general form, can be defined as miniaturized mechanical and electro-mechanical elements (i.e., devices and structures) that are made using the techniques of microfabrication [2]. The physical dimensions of MEMS devices can vary from the submicron region up to several millimeters. One main criterion of such microsystems is that there are at least a few elements having some sort of mechanical functionality.

MEMS can be divided into its functional elements which are miniaturised structures, sensors, actuators and microelectronics. In terms of its commercial importance microsensors and microactuators are found in everyday devices such as Smartphones and automobiles. In the case of a microsensor, the device converts a measured mechanical signal into an electrical signal. In a microactuator an electrical signal is applied which results in a mechanical response in the device where it is implemented [3]. To achieve such complicated microelectronic systems adapted deposition techniques from semiconductor manufacturing are applied. Thereby the quality of the micro-fabricated MEMS needs to match the today's requirements in terms of miniaturisation with constant device robustness.

Figure 1 shows a micro machined MEMS device which illustrates a suspension platform for optoelectronics under tension. The silicon dioxide layer acts as a mechanical stable platform layer for the germanium film and the tensile strained Silicon nitride (Si_3N_4). Due to the needed massive tensile stresses needed in Si_3N_4 to induce photoluminescence in Germanium one can understand the high mechanical requirements in terms of USG films [4]. In other MEMS structures USG films are used for different purposes in the same microelectronic device. This can implies thermal and electrical insulation layer, passivation layers and sacrificial films for photoresist patterning [5].

Such microelectronic devices are often implemented in areas with environmental challenges. This can be in the automotive sector where sensors are exposed to large temperature differences during the year.

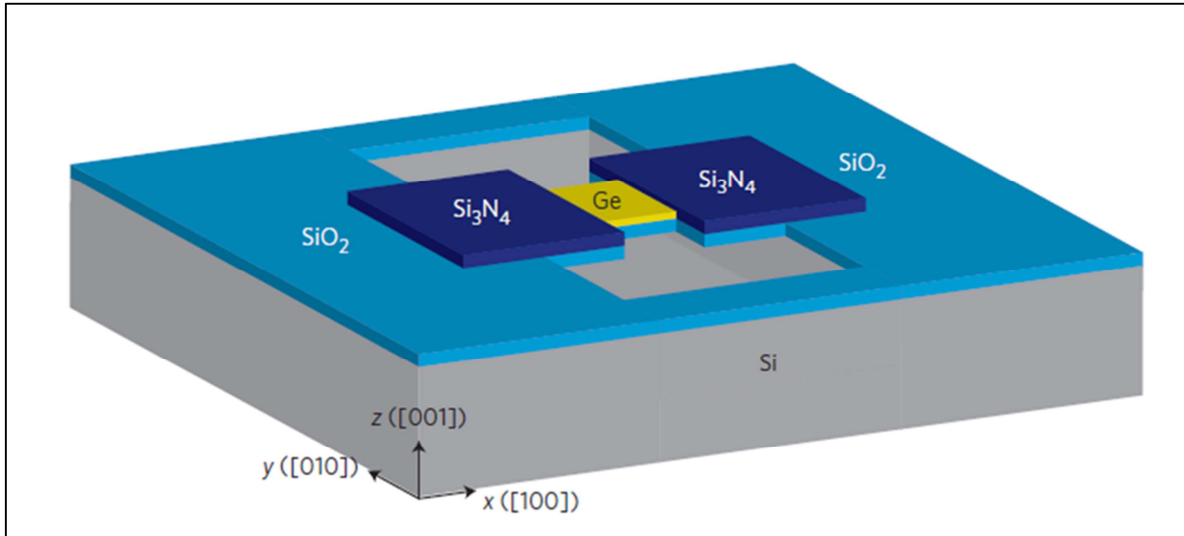


Figure 1: Micro machined MEMS device for optoelectronic applications where USG films are used as mechanical supporting layers for Si₃N₄ and Germanium [4].

Due to mechanical stresses caused by different coefficients of thermal expansion, high quality thin materials and suitable deposition principles are required. Therefore, one can imagine that the microfabrication of such layers plays a crucial role in terms of the mechanical stability.

1.3. Fundamentals of SiO₂

The undoped silicon glass microfabricated thin films for semiconductor applications are chemically the equivalent of quartz, which is a transparent crystalline solid used for oscillators and other optical devices [6]. Besides its similar optical properties, USG exhibits an amorphous structure compared to quartz. This means that SiO₂ exhibits no long range ordering like crystalline materials. Therefore, micromechanical phenomena, which occur during temperature processes, cannot be explained via classical elasto-plastic models which were developed for polycrystalline materials like thin copper and aluminium films (see Section 1.6, explanation of stress temperature curves of an aluminium thin film).

Table 1 summarises the most important properties of amorphous silicon dioxide. Since the properties of deposited USG films strongly depend on the deposition parameters and on the measurement techniques for thin film investigation, the table below gives information about the properties of bulk silica glass.

Table 1: Properties of USG as bulk material [7]

Undoped Silicon Glass	
stoichiometric composition	SiO ₂
Density	2.20 g/cm ³
Refractive Index	1.46 (600nm)
Elastic Modulus	70 GPa
Vickers Hardness	6.18 GPa
Poisson Ratio	0.17
Coefficient of Thermal Expansion	5.5x10 ⁻⁷ /°C
Thermal Conductivity	1.38 W.m ⁻¹ .K ⁻¹ (300K)
Dielectric Constant	3.8

In order to understand to provide a deeper understanding in terms of the amorphous arrangement found in silica glass, Figure 2 provides detailed information about bonding in amorphous SiO₂. As shown in Figure 2a, silica glass consists of nearly perfect SiO₄ tetrahedra joined together at the corners in various orientations. The bonding between the silicon (Si) and oxygen (O) atoms exhibits a strong covalent bonding character. This directional bonding leads to a short range order with each Si and four and twofold-coordinated oxygen[8]. Each O atom acts as a bridging atom between the neighbouring tetrahedrons. The angle between two neighbouring

tetrahedrons (Si-O-Si) is called the β bond angle. The β angle can vary from 100° to 180° with little changes in the bond energies. Torsion angles α_1 and α_2 are respectively the azimuth angles between the Si-O and the Si-Si (Figure 2b) [7].

The geometrical structure concept of silica glass is shown in Figure 2c. Considering theoretical concepts of amorphous network structures the most accepted theory is the random network hypothesis originally stated by Zachariasen and proofed by Warren et al via X-ray experiments [9],[10]. The glass network displayed in Figure 2 consists of randomly connected SiO_4 units. Possible ring structures (3, 5 and 7-membered rings) indicate the lower density (compared to the crystalline equivalent quartz), and explains the high degree of freedom of the bond angle.

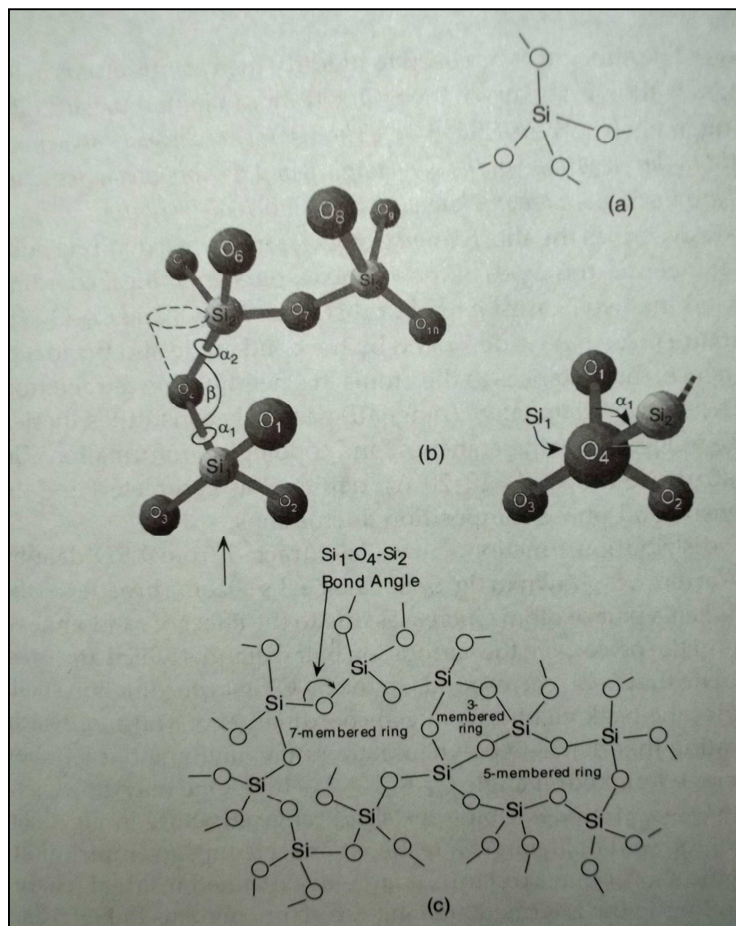


Figure 2: Structural properties of SiO_2 which displays the tetrahedral SiO_4 unit (a), the bond arrangement and the corresponding angles between silicon and oxygen (b) and a schematic structure model of glass(c) [7].

1.4. Deposition process of amorphous Silicon dioxide

USG is the most common and oldest microfabricated dielectric material in the microelectronics industry. Many processes exist to achieve the film composition of SiO_2 . Most of the modern sophisticated chemical vapour deposition (CVD) technologies were developed in order to meet the production requirements such as quality, uniformity, composition reproducibility, and particle free surfaces for SiO_2 . To fulfil these requirements nearly all USG is deposited by CVD processes and plasma enhanced CVD (PECVD) processes. Since aluminium is very often used as metallisation layer in microelectronic devices, subsequent deposition processes after such metallisation layers have to run at lower temperatures. Otherwise, diffusion processes and melting of metal layers would occur, since the melting point of aluminium is at 660°C . Furthermore, temperatures below 450°C are preferred to prevent thermal activated diffusion processes of dopants in silicon. Hereby PECVD processes can achieve deposition temperatures between $150\text{--}400^\circ\text{C}$ depending on the used deposition parameters. The needed activation energy for the chemical reactions for film deposition is partly provided by an electrical gas discharge (a physical plasma) in the deposition chamber, which excites the precursor molecules. In classical CVD process the needed reaction enthalpy is supplied by high substrate temperature, leading to higher temperatures compared to PECVD [11]

As previously mentioned, PECVD processes achieve much lower temperatures compared to classical CVD processes and are very suitable for inter-metal dielectrics. The required energy for the decomposition of the precursor gases into neutral and ionised species and chemical reactions on the substrate surface are supplied by the physical plasma. The molecular species become kinetically activated through collision processes in the plasma and reduce the deposition temperature significantly [12].

In many applications the additional energy is supplied by a radio frequency (RF) induced glow discharge. Normally this is a non-thermal plasma and its gas species are not in thermal equilibrium ($T_{\text{electrons}} \gg T_{\text{ions}}$). In Figure 3 the schematic arrangement of a parallel-plate reactor is shown. The plasma power is supported by capacitive coupling between the heater plate and the showerhead. The purpose of the matchbox is to pass the RF power from the power supply to the plasma load. The match network introduces variable inductance and capacitance between the generator and the plasma load so when adjusted properly a resonant circuit is formed [1]. To maintain the glow

discharge a low pressure of several Torr is required. Therefore, a high pumping speed is needed to achieve low pressures at high gas flow rates. The precursor and carrier gases flow into the chamber over the showerhead. The hole patterns were designed to optimise the gas distribution and the material transport over the wafer.

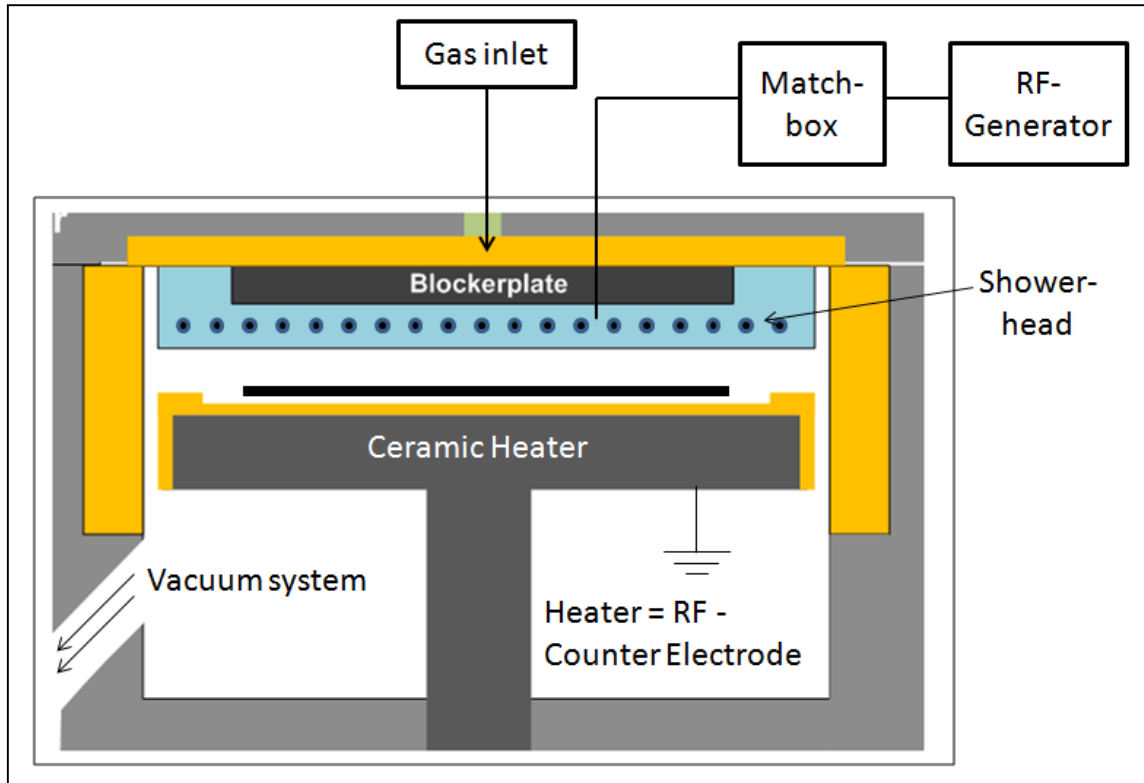


Figure 3: Schematic process chamber of the PECVD silane deposition. Silicon substrate is heated via a ceramic heater plate. Additional energy is supplied via RF-plasma which activates the incoming gas stream.

To describe the fundamental steps in a PECVD chamber during deposition one has to be aware that all of the reaction steps are strongly dependent on the process parameters (e.g. pressure, gas flow, substrate temperature, etc). Figure 4 gives a simplified overview of the PECVD process, which can be divided into *plasma activation*, *transport phenomena in the gas phase* and *surface reactions*. The activation in the plasma is primarily due to collisions with highly energetic electrons which creates excited precursor molecules and different forms of free radical species. A minor fraction of the precursor molecules are ionised but due to the higher potential energies only a low probability. The activated species can then diffuse directly to the substrate surface (4b), react with other radicals or molecules (4c) which then diffuse to the surface (4d). Depending on the plasma characteristics some source gases reach the surface without any plasma activation (4e) or are pumped away directly (4f).

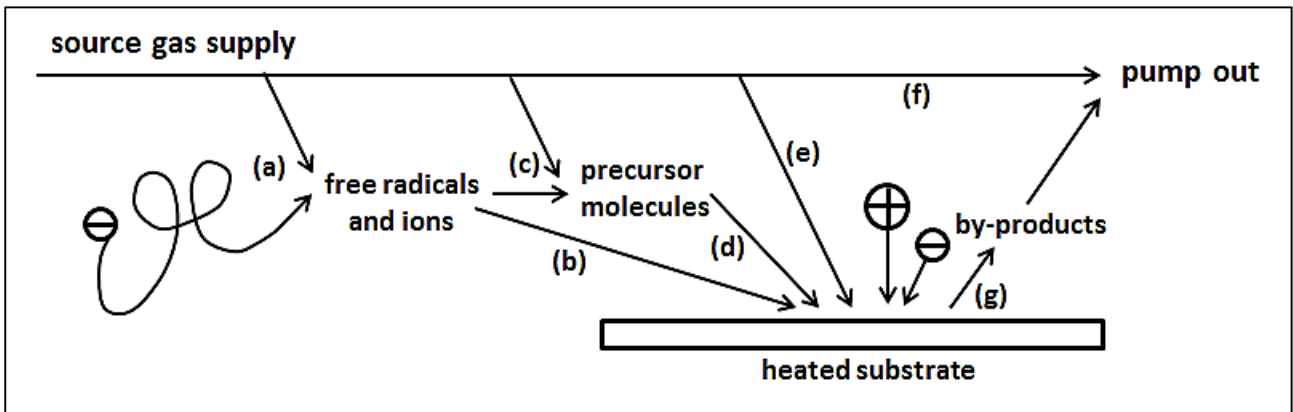
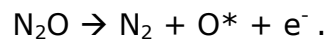


Figure 4: Basic transport scheme of reactant gases to the substrate surface.

After the reactant gas species are physisorbed onto the wafer they may migrate or diffuse on the surface until they bind to an energetically favourable site, until they desorb from the surface, or until they react chemically with another reactant species to the desired film molecule and start film nucleation. At the same time by-products desorb from the surface and are pumped out (4g) [13]. These different surface reactions are activated by electron and ion bombardment from the surrounding RF glow discharge and by the substrate temperature, T_s . Therefore, it is obvious that the optimum parameters for film growth are adequate deposition temperature/plasma energy for chemical surface reactions and sufficient reactant species on the wafer to form stable nuclei.

Limitations of film growth also occur due to insufficient mass transport of activated precursor gases to the substrate surface which is given by gas flow and plasma characteristics. PECVD process parameters in the semiconductor industry are often empirically optimised due to the diversely complicated parameter-relationships.

The deposition recipes using plasma assisted processes strongly depend on the used parameters. As it is impossible to display every occurring reaction of the overall process, this section only provides general information about the deposition of silane based silica glass. The deposited silane based USG films of this study were processed using nitrous oxide (N₂O) as gas for the plasma generation and as the parent donor molecule for oxygen atoms which can be stated as

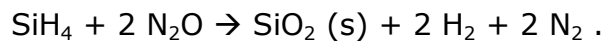


The dissociative excitation of nitrous oxide is the fundamental reaction for the oxygen supply and maintenance of the glow discharge. The activation energy for the reaction can be supplied by inelastic collisions with other gas species or collision with electrons.

The deposition rate limiting gas in the chosen process is the silane (SiH₄) gas which functions as the silicon (Si) source. Via plasma activation processes silane can be completely decomposed into



Through diffusion processes the reactive species move to the surface leading to the overall intended chemical reaction of



Since the overall reaction gives only information about the target composition of the glass film, one can assume that the reaction kinetics are much more complicated. Plasma reactions between SiH_x (x = 0–4) species and N·, NH· or NH₂· radicals and various reactions between Si and O-containing species have to be considered. Based on the process parameters (pressure, substrate temperature gas flow ratios, etc.) different species like polysilanes (i.e. SiH₃O, SiH₂ON, HSiO₂N, etc.) as well as molecular species of hydrogen, nitrogen and oxygen can be deposited [12]. For predicting reactions in thin film deposition, Kinetic Monte Carlo simulations are often applied [14]

1.5. Mechanical Stresses in amorphous thin Film processing

Since it is possible to produce thin solid films on various substrates the resulting stresses in these layers has been a major concern. Especially because stress evolution in thin films is not comparable with bulk materials due to the high surface to volume ratio and the stronger influence of the microstructure and the interface between thin film and substrate [15],[16].The existence of internal stresses in films has been known since 1858 when the English chemist Gore noted that his electrodeposited thin films had a concaved shaped oriented to the cathode side [17]. Since then the origins of film stress have been investigated in order to understand and control stresses of thin films deposited on a substrate. Figure 4 shows the effect of thin film stress which can result in either tensile or compressive states.

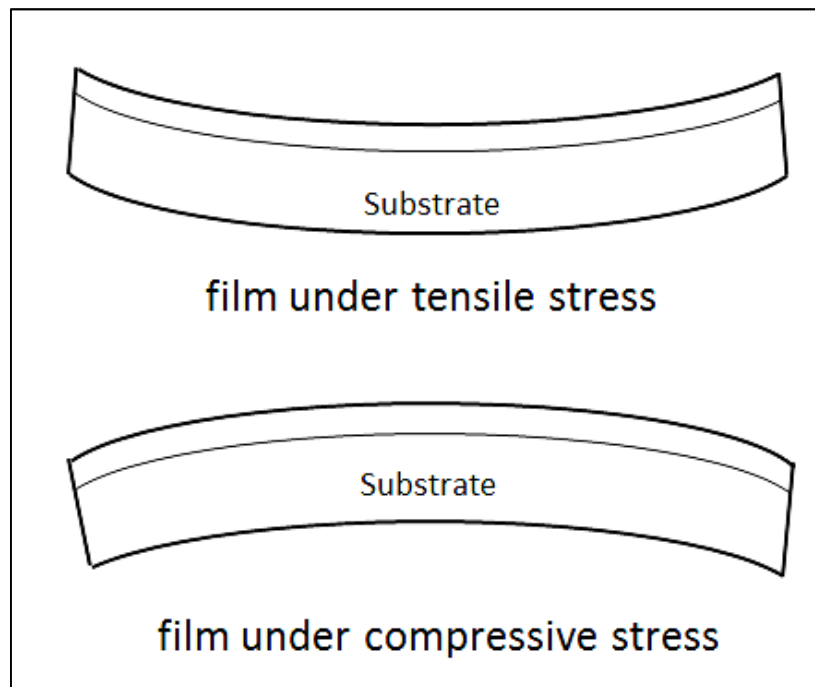


Figure 5: Schematic illustration of a thin film deposited on a substrate which can result in tensile or compressive film stresses.

Stresses in thin films can be seen as two separate parts, thermal stresses σ_t and intrinsic film stresses σ_i resulting in an overall equation:

$$\sigma = \sigma_t + \sigma_i . \quad (1)$$

As mentioned in Section 1.3 amorphous materials have no long range order due to their lack of a crystalline lattice. This leads to the conclusion that stresses in thin amorphous films lead to different phenomena compared to crystalline materials.

Intrinsic stresses which are generated during the deposition processes can be compensated via relaxation process like dislocation movement or hillock formation [18]. In amorphous and brittle materials the generated film stresses often result in crack formation.

The origin of thermal stresses is based on the different coefficients of thermal expansion (CTE) between the thin film material and the substrate. Films and coatings prepared at elevated temperatures and then cooled to room temperature will be thermally stressed due to the constrained nature between the thin film and the substrate. The film stress which is caused by thermal effects can be stated as followed:

$$\sigma_t = E_s \cdot (\alpha_f - \alpha_s) \cdot (T_D - T_C). \quad (2)$$

Hereby, the thermal stress is obtained the elastic modulus of the thin film, E_s , the linear thermal expansion coefficients of the film material, α_f , and the substrate, α_s , as well as the difference between the deposition temperature, T_d , and the current temperature, T_c . Films prepared at elevated temperatures will be residually compressed when measured at room temperature if $\alpha_s > \alpha_f$, since the substrate shrinks more than the film material.

To actually measure the thin film stress, σ , of the desired film-substrate composite the mechanical problem has to be transformed into a mathematical model. Gerald Stoney was the first person who stated a relationship between biaxial bending and resulting stresses in thin films [19]. Regardless of the internal stress distribution the maintenance of the mechanical equilibrium of the film-substrate requires that the net force (F) and the bending moment (M) vanish on any film/substrate cross section. This leads to

$$F = \int \sigma \cdot dA = 0 \quad (3)$$

and

$$M = \int \sigma \cdot y \cdot dA = 0, \quad (4)$$

where A is the sectional area and y is the moment lever arm. With these basic equations one can derive Stoney's equation. This thin film stress equation can be derived with reference to Figure 6. The film/substrate combination (6a) indicates the mechanical problem of interest where h_f and E_f are the thickness and the elastic modulus of the film, with corresponding substrate values of h_s and E_s . In Figure 6b

each interfacial set of forces can be replaced by the statically equivalent combination of a force and moment which leads to F_s and M_s in the substrate and F_f and M_f in the film, where $F_s = F_f$.

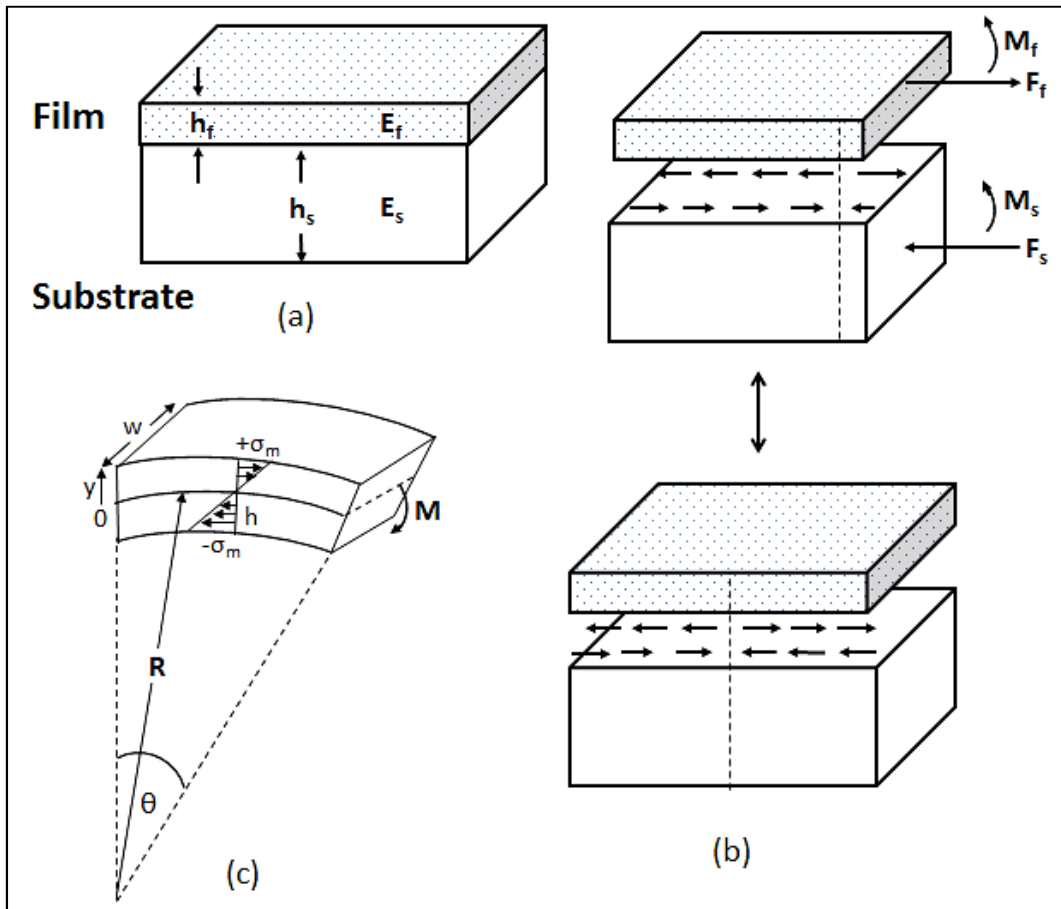


Figure 6: Stress analysis of thin films. (a) displays the thin film/substrate composite. (b) indicates the interfacial forces and moments of the film and the substrate displayed as simple plates, (c)

Considering a free body beam bent by moment M as indicated in 6c. The stress distribution reflects this by varying linearity across the section from maximum tension ($+\sigma_m$) via zero neutral axis to maximum compression ($-\sigma_m$). The moments are responsible for the biaxial bowing of the film-substrate combination. The strain response is then related to a curvature radius via the Hook's law. Since h_s is normally much larger than h_f , the film stress σ_f is, to a good approximation given by the Stoney's equation

$$\sigma_f = \frac{1}{6.R} \frac{E_s \cdot h_s^2}{(1-\nu_s) \cdot h_f} \quad (5)$$

where R is the radius of the film substrate composite and ν_s the Poisson's ratio of the substrate [18].

1.6. Wafer Curvature Method

The wafer curvature method is an optical in-situ stress measurement method used especially in the microelectronics industry to monitor wafer stresses. It measures the curvature of the film-substrate system which is then transformed via Stoney's equation (eqn. 5) into a stress value [20]. To measure the induced curvature during a heat treatment or deposition process the curvature has to be determined accurately. Therefore, a multi-beam optical sensor (MOS) technique is the very often used. The schematic setup of a wafer curvature with MOS technique is shown in Figure 7. A laser beam is focused via optical lenses and is passed through two etalons, which are similar to a Fabry P rot Interferometer, to divide the laser beam into a two dimensional laser beam array (two etalons because of x and y -directions). The beam array is then directed to surface of the wafer, reflected back and then detected in the charged coupled device (CCD) [21].

The change in curvature is $\kappa - \kappa_0$, where κ_0 is the initial curvature, and is connected to a stress change via Stoney's equation. If the surface is completely flat, the beams will have the same spacing after being reflected as they had in the incident beam array. When the sample has a certain curvature, the beams will be deflected and the spacing of the beams on the CCD will be different [21]. Therefore, the spacing between the beams is a direct measurement of the substrate curvature. In Figure 7 the geometric relationship between curvature and beam deflection is shown.

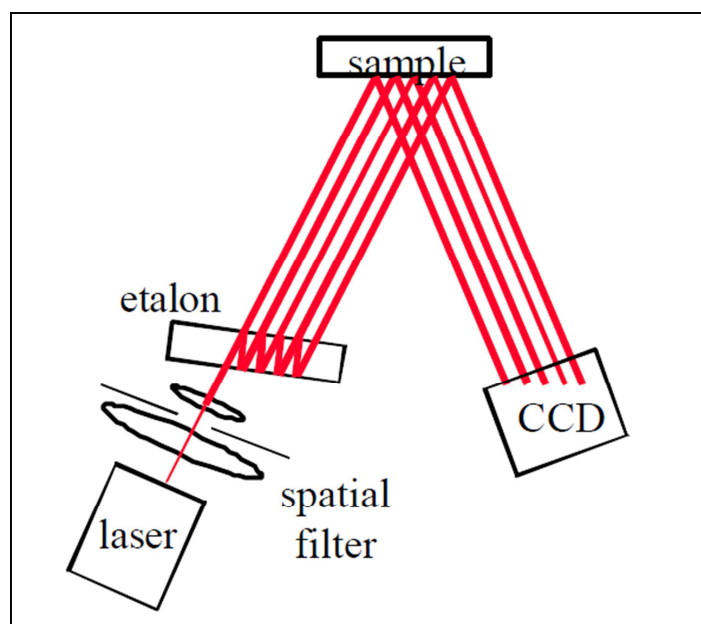


Figure 7: Schematic illustration of the used KSA multi-beam optical sensor (MOS). A laser beam array is generated via optical devices, which is reflected by the sample and detected using a charge coupled device (CCD) detector [22].

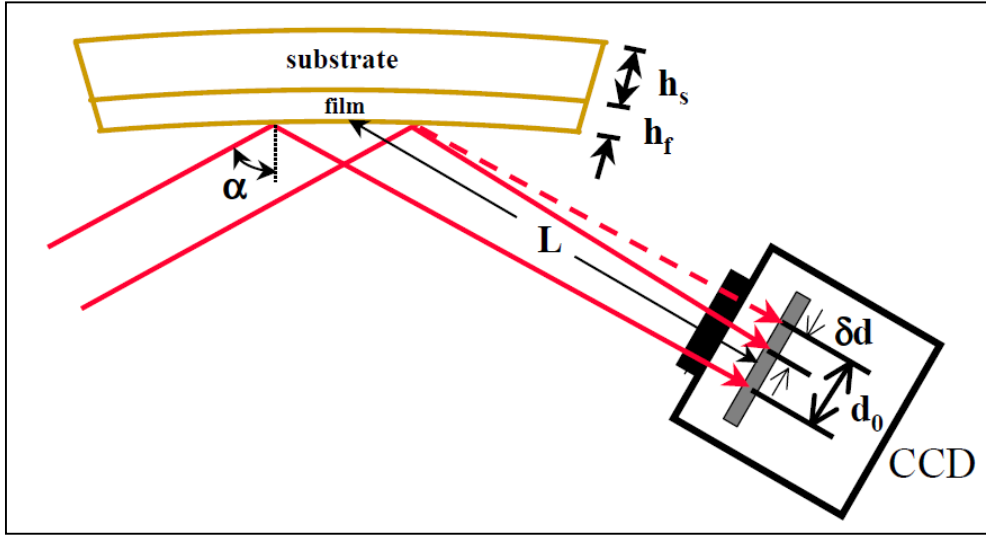


Figure 8: Basic relationship between the sample curvature and the measured beam deflection [21].

Mathematically the difference in curvatures can be seen as

$$\kappa - \kappa_0 = \frac{\delta d}{d_0} \frac{\cos \alpha}{2L} \quad (6)$$

where δd is the difference in beam spacing from the initial spacing d_0 , due to the stress induced curvature, L is the distance of the sample to the camera and α is the angle between the laser beam array and the sample (see Figure 8). Combining the mathematical relationship of laser deflection with the well-known Stoney formula shows that the measured stress is directly proportional to the measured beam deflections given by

$$\sigma \cdot h_f = \frac{\delta d}{d_0} \cdot \frac{h_s^2 M_s \cos \alpha}{12L} \quad (7)$$

Figure 9 represents a typical wafer curvature experiment of a thin aluminium film [23]. Polycrystalline metal films exhibit hysteretic stress responses during thermal cycling due to a thermal mismatch between the film and substrate is relaxed by creep deformation processes at elevated temperatures. A typical stress-temperature response includes compressive thermal stress development upon heating, which is described as thermoelastic behaviour (room temperature – 200°C). This is followed by relaxation to near zero stress at high temperatures. Such relaxation processes are temperature dependent mechanisms like grain growth, dislocation movement, creep deformation, and grain boundary relaxation, which lead to plastic deformation of the thin film (200°C-450°C). During cooling tensile stresses are developed due to thermal

mismatch of the substrate (silicon) and the thin film material (polycrystalline aluminium) [24].

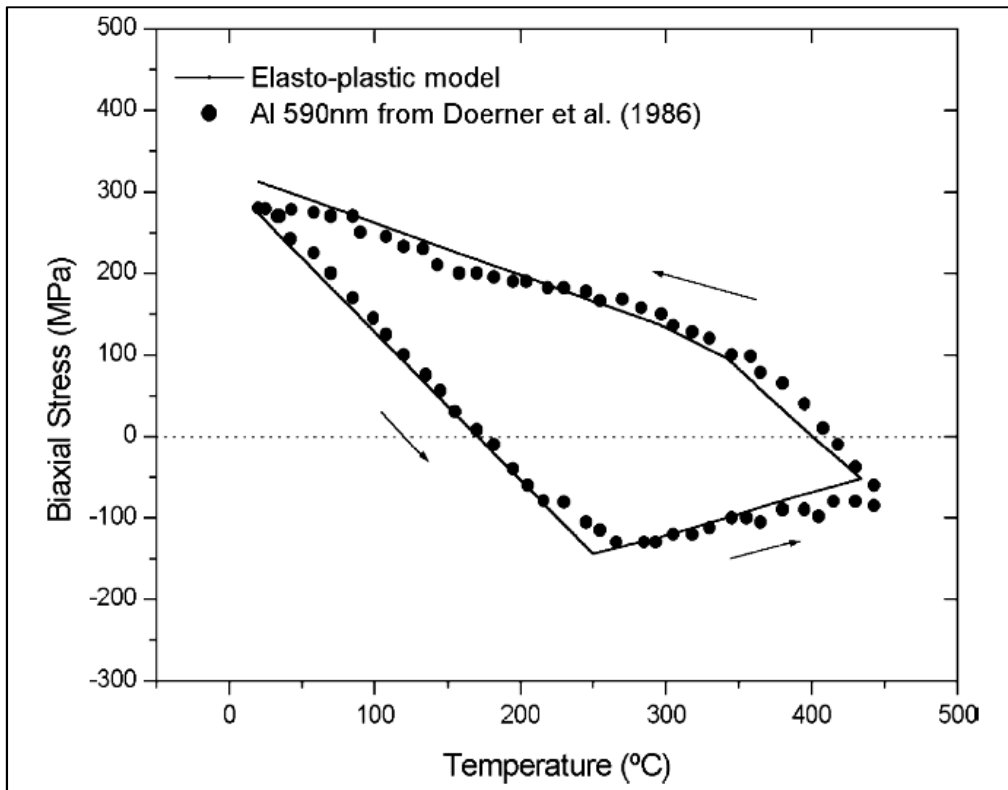


Figure 9: Typical Stress-temperature data of a polycrystalline aluminium film deposited on a silicon substrate. The thermocycle indicates linear compressive stress generation due to CTE mismatch and following relaxation events in aluminium [23].

1.7. Fourier Transform-Infrared Spectroscopy

Infrared spectroscopy is a powerful analytical tool to measure the bonding characteristics and the chemical structure of thin films. A FT-IR spectrometer has a beam containing many frequencies of light at once and measures how much of that beam is absorbed by the sample. For the analysis of molecule vibrations the infrared range of 2.5-25 μm wavelength (4000-400 cm^{-1}) is used because it is energetically in the same range of the excitation energies for most of the vibration modes between the atomic bonds [25]. The chemical information of the sample is an interferogram which is created by a Michelson Interferometer (see Figure 10).

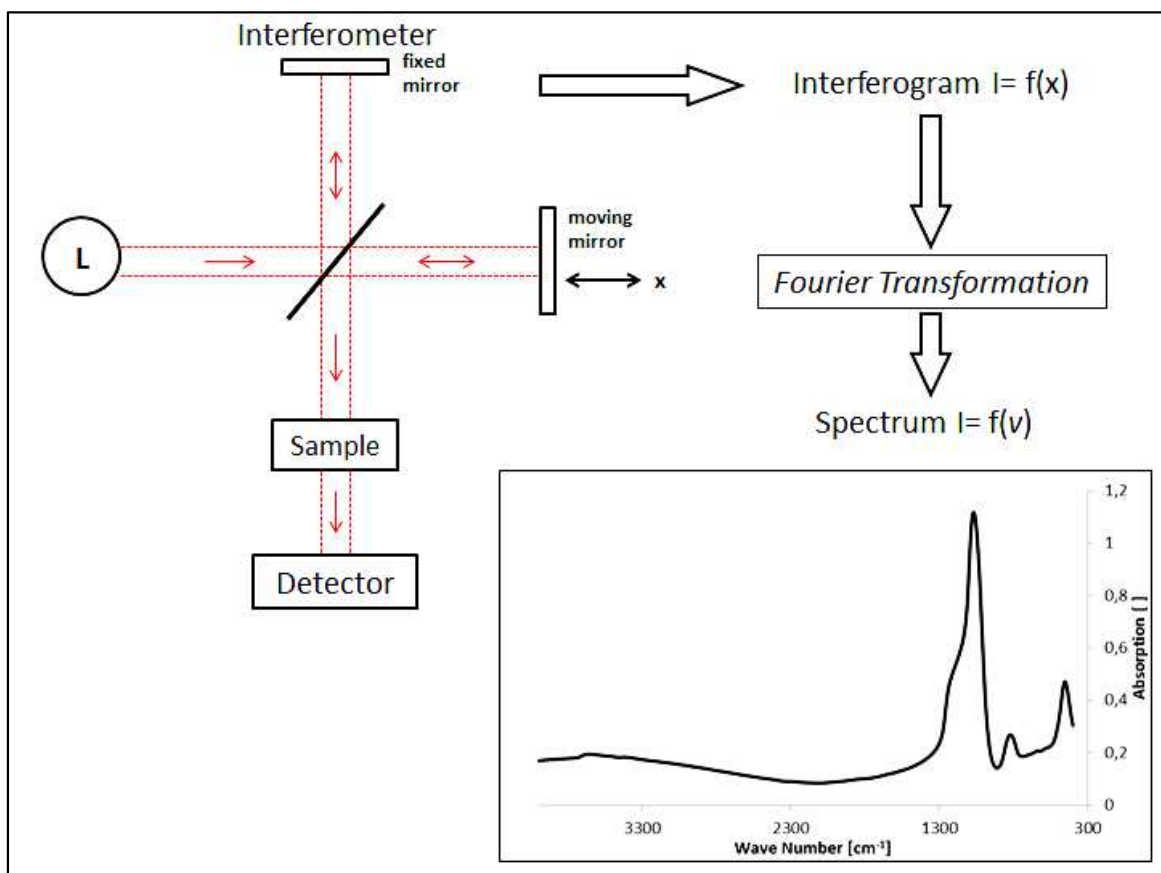


Figure 10: Basic scheme of FT-IR processing. The sample is exposed to a beam of light in an interferometer which creates a specific interferogram. Via a Fourier transformation a spectrum is obtained where the signal is a function of the wave number.

In order to get the continuous spectral information (absorption/transmission behaviour) of the material in the used frequency range a common algorithm called the Fourier transform is applied. It turns the raw data (light absorptions for each mirror position) into the specific material absorption spectrum (light absorption for each wavelength) [25].

Figure 11 shows an absorption spectrum of a silane based USG film measured with an in-line spectrometer. For the SiO_2 film characterisation three characteristic IR absorption bands which occur at energies of approximately 1075, 800 and 450 cm^{-1} were identified. These correspond to the stretching, bending and rocking motions of two-fold coordinated oxygen atoms in a thermally grown SiO_2 film. The energy of the stretching vibration varies with composition and, therefore, this band is used as a quality indicator in terms of the SiO_x stoichiometry ($x=0-2$; $x=0$ oxygen impurities in amorphous Si with 940 cm^{-1} ; $x=2$ stoichiometric SiO_2 with 1075 cm^{-1}) [26],[27]. The addition of impurities of nitrogen and hydrogen species leads to additional vibrations and energy shifts which is explained in more detail in Sections 2, 3 and 4.

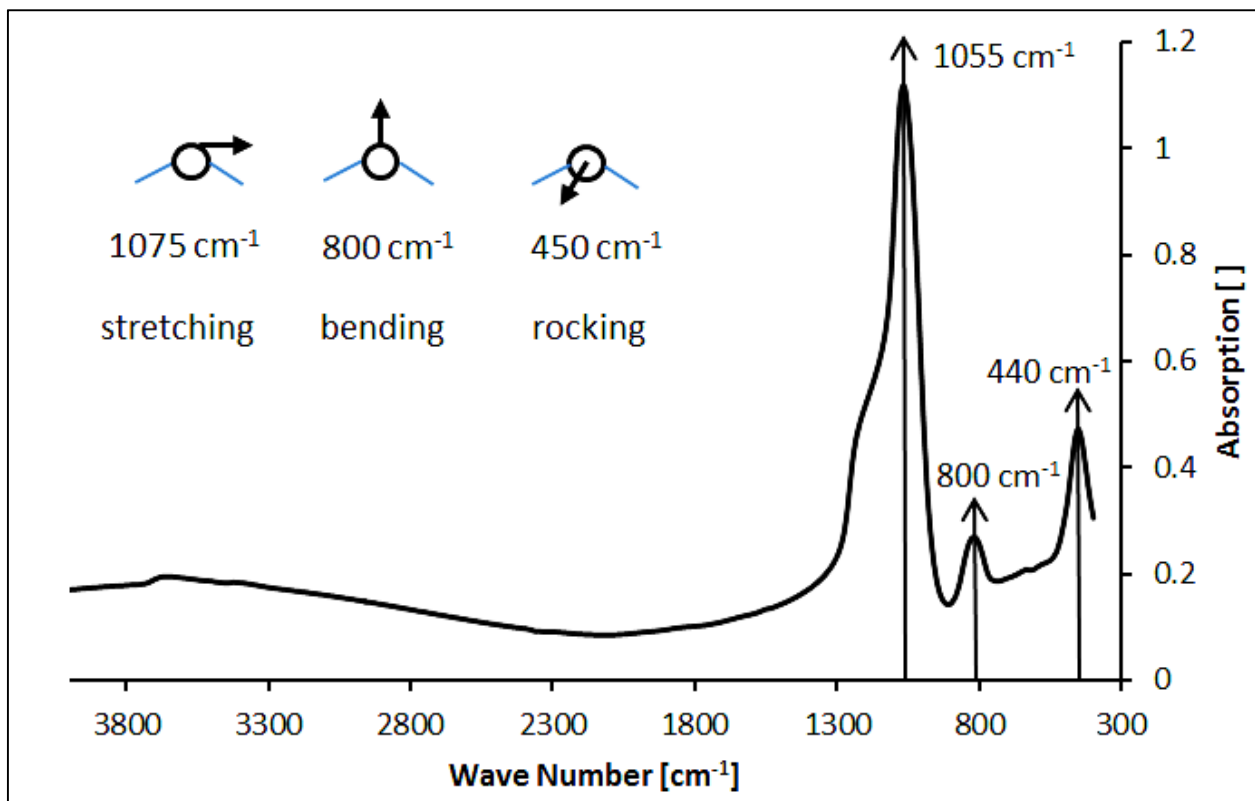


Figure 11: FT-IR absorption spectrum of a silane based USG film. The vibration modes displayed on the graph indicate the motion of the oxygen atom in the stretching, bending and rocking vibration modes with the corresponding energies for a stoichiometric SiO_2 film compared to the three labelled wave numbers from a PECVD deposited USG film.

1.8. Nanoindentation

In the last two decades the mechanical characterisation of thin films or other small volumes of materials has gained much interest. A new depth sensing indentation method, evolved from micro/macro indentation was developed to obtain values for elastic modulus and hardness using readings of indenter load and depth of penetration at the nanometer scale [28]. The difference compared to micro-hardness testing is that the residual indentation area (area of indent) is not measured with light microscopy. Instead, the relationship between the well-known geometry of the used indenter tip and the depth signal from the transducer is converted to an indent area. Therefore, it is very important to calibrate the residual area of the indenter tip in terms of the contact depth. This is often referred to the empirical (polynomial) area function of the used tip (projected area versus contact depth).

During indentation a load-displacement curve is created which then can be used to extract the mechanical properties of elastic modulus and hardness of the material. From the initial unloading slope, dP/dh of the unloading curve (see Figure 12) one can obtain the stiffness, S , of the elastic contact. It is then used to calculate the reduced Young's modulus, E_r ,

$$E_r = \frac{1}{\beta} \frac{\sqrt{\pi}}{2} \frac{S}{\sqrt{A_p(h_c)}}, \quad (8)$$

where h_c is the contact depth, β is a geometrical constant of the tip and $A_p(h_c)$ is the projected area of the indent at the contact depth. For indentation hardness the relationship

$$H = \frac{P_{max}}{A_p} \quad (9)$$

is used where the maximum applied indentation load, P_{max} , is divided by the projected contact area, A_p , of the tip at maximum load [29].

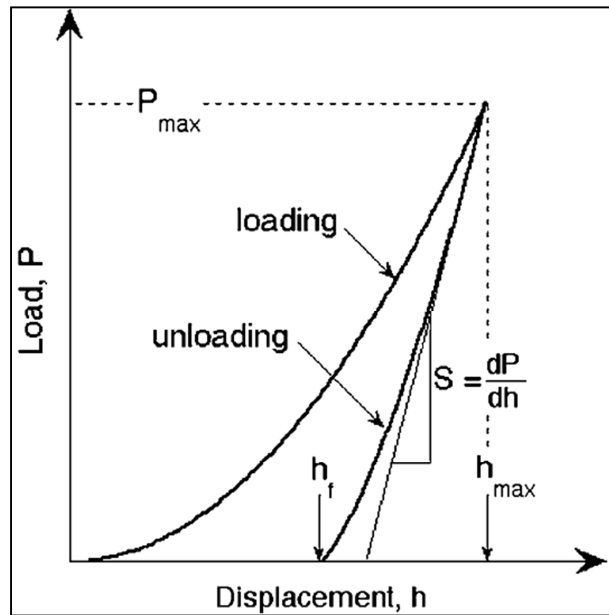


Figure 12: Load-displacement curve indicating the determination of the stiffness in the unloading curve [29].

When an indent is made into a thin film on a substrate there is a volume underneath the indent that is affected and used in the analysis of property determination (see Figure 13). If this affected volume has also a fraction of the substrate interacting with it then the properties of the substrate can influence the measured properties of the thin film itself; thus giving mechanical properties close to the substrate and not the film that is being tested [30]. Therefore, only small sample volumes are used to overcome this problem (which means small indent depths compared to the film thickness). This enables accurate measurements of the film's properties and not the substrate's properties.

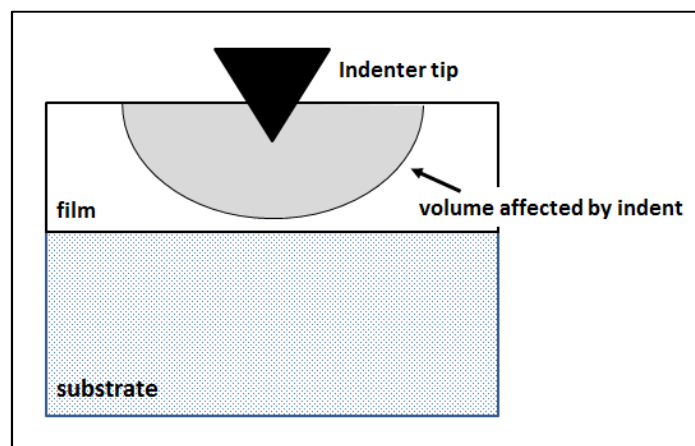


Figure 13: Affected volume during indentation made in a thin film sample [30].

2. Experimental and deposition results

All wafer fabrication tasks were performed at the production site of Infineon AG Austria in Siemensstraße 2, 9500 Villach. Therefore, all equipment for deposition process and quality analysis of the films was completed with available production equipment.

2.1. Film deposition and characterisation

In order to investigate the influence of high hydrogen and nitrogen impurities two different deposition processes were created. One deposition process resulted in a high content of hydrogen and nitrogen and another which improved the deposition process in terms of stress behaviour. Four deposition parameters were chosen to alter the properties of the USG films. These were the precursor gas flow for the silicon supply silane (SiH_4), ammonia (NH_3) gas flow as the artificial nitrogen source, the spacing between heater plate and showerhead and the input plasma power. These two film systems were compared with the current production recipe of the silane USG process to evaluate the differences in stress, chemical and mechanical changes as a function of thermal treatment. Finally, the production deposition process for the TEOS (Tetraethoxysilane) USG process was put into the experimental approach to evaluate the differences of the usage of a different precursor in terms of the investigated properties. Table 2 gives a summary of the used films with the corresponding parameters. Film A has a high nitrogen and hydrogen content, Film B was the optimised film (N and H free), Film C was the current USG silane standard process in production and Film D was the current USG TEOS standard process. The silane based films were deposited with an Applied Materials Producer, whereas the TEOS based USG film was deposited with an Applied Materials P5000.

Table 2: Deposition parameters of Films A, B, C and D

deposition parameters: silane based films							
Film-System	Heater-Temp. [°C]	Pressure [Torr]	N ₂ O [sccm]	SiH ₄ [sccm]	NH ₃ [sccm]	Spacing [mils]	RF [W]
A	400	2.7	3900	320	100	430	200
B				200	0	630	400
C				255	0	540	270
deposition parameters: tetraethoxysilane based film							
D	430	8.5	2900	1320	1000	250	700

Deposition of the dielectric films itself occurred on standard 8 inch silicon (100) oriented wafers with an average thickness of 725 μm . All wafers were cleaned and tested in terms of particle density to meet the requirements of standard wafer fabrication. Table 3 summarizes the obtained film deposition results from the inline measurements. As one can see in Table 3, the deposition time was adjusted for each film system so that an approximate thickness of 1000 nm (1 μm) was obtained. The thickness and the refractive index of the deposited films were measured with an ellipsometer at 670 nm.

Table 3: Initial film properties which were obtained at the plant side

initial properties: silane based films							
Film-System	Deposition Time [s]	Thickness [nm]	Dep. Rate [nm/s]	Range [nm]	Uniformity [%]	RI [-]	Stress [Mpa]
A	49	988	20.16	10	0.51	1.5182	72
B	152	1010	6.64	51	2.52	1.4603	-194
C	64	1006	15.56	35	1.76	1.4608	-95
initial properties: tetraethoxysilane based film							
D	49	988	20.16	10	0.51	1.4639	-128

The general definition of the refractive index itself, is a dimensionless number which gives the ratio of the propagation speeds of an electromagnetic wave (with a certain frequency) in vacuum compared to a medium (physical matter) [31]. For dielectric materials the refractive index plays a key role in respect to the macroscopic physical properties. The refractive index provides information about the interactions of electromagnetic waves (e.g. light) and physical matter (e.g. glass films). The electric field of a plane electromagnetic wave induces oscillating dipoles in a material, and these oscillating dipoles give feedback on the electric field to make the wave propagate at a different speed than it would in vacuum. In the case of a dielectric medium, electrons are subject to an elastic restoring force that keeps each electron bound to its respective atom and a damping force that dissipates energy and gives rise to absorption (Lorentz Model of Dielectric, late 1890s) [32]. Hence the refractive index depends on the compositional and structural properties. Films B, C and D had a refractive index of 1.46, which is the same value found for the stoichiometric silica glass (see table 1). Film A had a distinctively higher refractive index of 1.52 which is an indication that the stoichiometry deviates from SiO_2 due to the presence of hydrogen and nitrogen species and the resulting non-stoichiometric composition of silicon and oxygen. The range and the uniformity parameters give the absolute and relative measurement variation. The film stress after deposition was measured with wafer

capacitance measurement. Films B, C, and D were in the compressive stress state, while Film A resulted in a tensile stress.

2.2. Sample preparation

To meet the geometric restrictions of the characterization instruments the coated wafers were cut into smaller samples. The wafers were cut on the uncoated backside using a diamond cutter. To ensure that samples can be broken into well-defined quadratic pieces the wafer notch was used as cutting orientation. This mark shows the $\langle 110 \rangle$ direction of the (100) Silicon wafer. Figure 13 shows a schematic example of the sample preparation. The wafer was scratched with the diamond cutter along two $\langle 110 \rangle$ directions which are orthogonal to each other. Subsequently some pressure was applied so that the small quadratic wafer pieces break apart. All the film samples were prepared with dimensions of $1.1 \times 1.1 \pm 0.1$ cm. Besides the geometric requirements of the analytical instruments the constant sample size ensures that no geometric contributions effect the measurements (e.g. different sample sizes for curvature measurements)

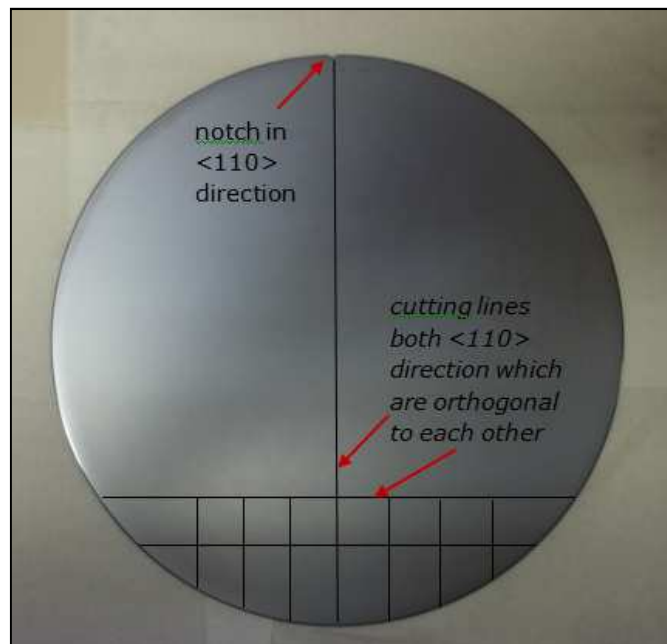


Figure 14: Back side of a coated 200 mm silicon wafer indicating the cutting lines.

2.3. FT-IR as-deposited results

Infrared spectroscopy is an analytical method for qualitative chemical and structural information. It provides information about the bonding characteristics and is used for creating a chemical fingerprint. To quantify molecular or atomic species one has to create a calibration method for the specific material which is connected with a high effort. Besides that a baseline correction and an appropriate algorithm for peak integration has to be used to obtain reliable results. Therefore, interpretation of the obtained FT-IR results was performed qualitatively for obtaining chemical and structural information of the four film systems.

The deposited films were characterised in terms of their chemical composition using a Nicolet Avatar 320 FT-IR spectrometer. Figure 15 shows the as deposited IR spectra. Significant differences between Film A and the other three film systems can be seen in the figure. The high concentrations of nitrogen and hydrogen species have a large impact on the spectral region of 4000 to 400 cm^{-1} . Nitrogen species in the form of Si-N-H and N-H species can be observed at around 3390 cm^{-1} . Nitrogen species were incorporated in the amorphous material by the artificial N-source ammonia (NH_3) and possibly by the precursor gas nitrous oxide (N_2O). This can be assigned to the partially decomposed N-H species from NH_3 gas and other by-products from the oxygen supply gas N_2O . Chapter 5 will give a more detailed discussion. At around 2200 cm^{-1} the Si-H stretch band appears. This is due to the incomplete oxidation or decomposition of the silane (SiH_4) precursor gas. The peak at 2350 cm^{-1} is the CO_2 stretch vibration and is formed due to local atmospheric changes during the measurement.

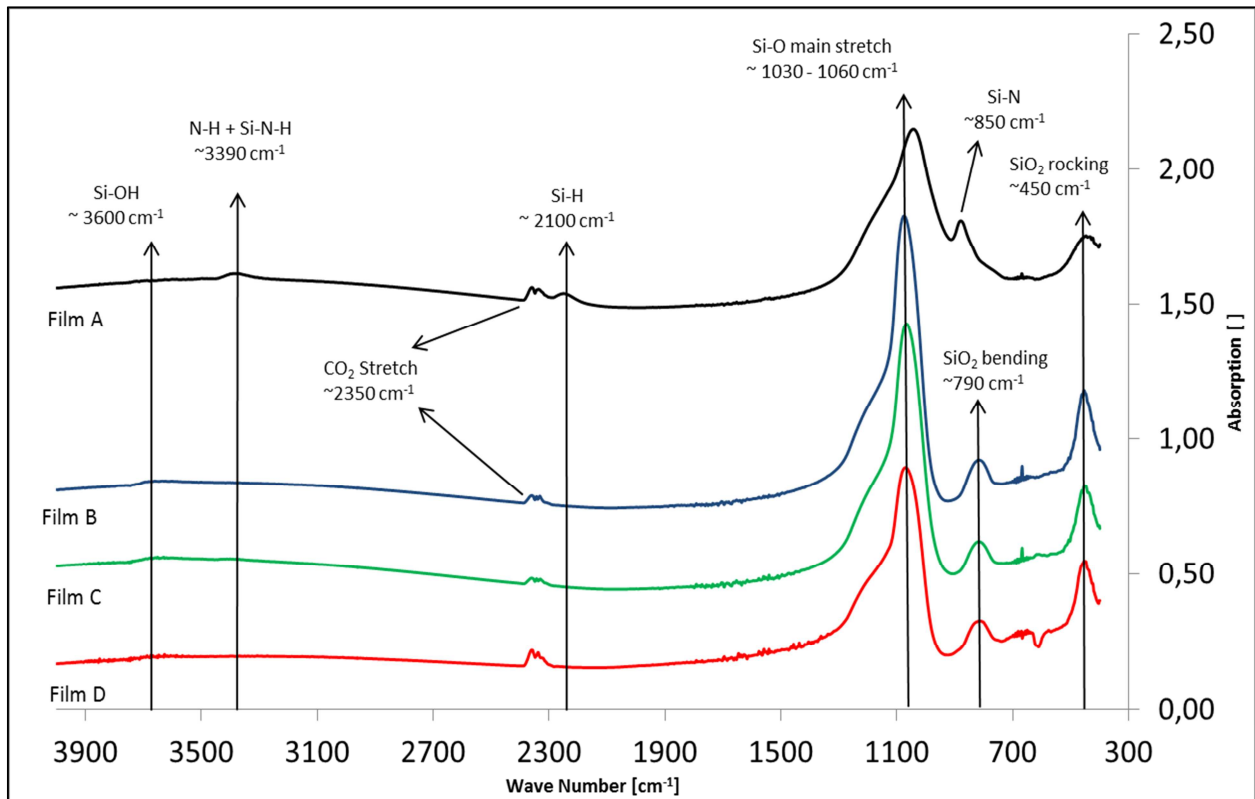


Figure 15: Infrared spectra of Films A, B, C and D. Film A reveals additional peaks due to nitrogen and hydrogen doping, whereas the other three films only exhibit minor impurities of silanol (Si-OH) groups.

Additionally, Films B, C and D can be seen as almost perfectly amorphous SiO_2 material because all of them show a sharp peak maximum at around $1070\text{-}1060\text{ cm}^{-1}$ which is the main Si-O stretch vibration and qualitatively describes the SiO_2 tetrahedral network. Therefore, this band was used to evaluate the quality of the obtained film by comparing it with the Si-O peak appearing in thermally grown SiO_2 at around 1080 cm^{-1} . The well-defined shoulder around $1200\text{-}1100\text{ cm}^{-1}$ spectral region corresponds to the Si-O-Si out-of phase stretching. In the presence of high N and H concentration the bonding characteristics of the dielectric film changed. The main Si-O stretch band broadened due to Si-N and Si-H bonds. This can be seen at around 850 cm^{-1} spectral region where a Si-N stretch peak appears in Film A. Furthermore, a significant band shift from the Si-O main stretch to higher energies around 1030 cm^{-1} is observed. The Si-O-Si bending vibration at around 790 cm^{-1} is significantly reduced and overlaid by the neighbouring Si-N band. This can be also observed at the high energy Si-O-Si rocking vibration band which appears in the spectral region at around 450 cm^{-1} . Films B, C and D show a sharp band, while with Film A the peak is much smaller and broadens due to symmetric stretch vibrations of Si-N around 490 cm^{-1} .

To provide a better understanding of the influence of high nitrogen and hydrogen concentrations in terms of the spectral changes Figure 16 provides detailed information about the differences between a standard production USG silane film (Film C) and Film A, which exhibits high N and H doping. Here, it should be mentioned that the production USG silane recipe, Film C, has a minor fraction of nitrogen incorporated which can be seen as a diminishing peak around 3400 cm^{-1} (see black circle Figure 16).

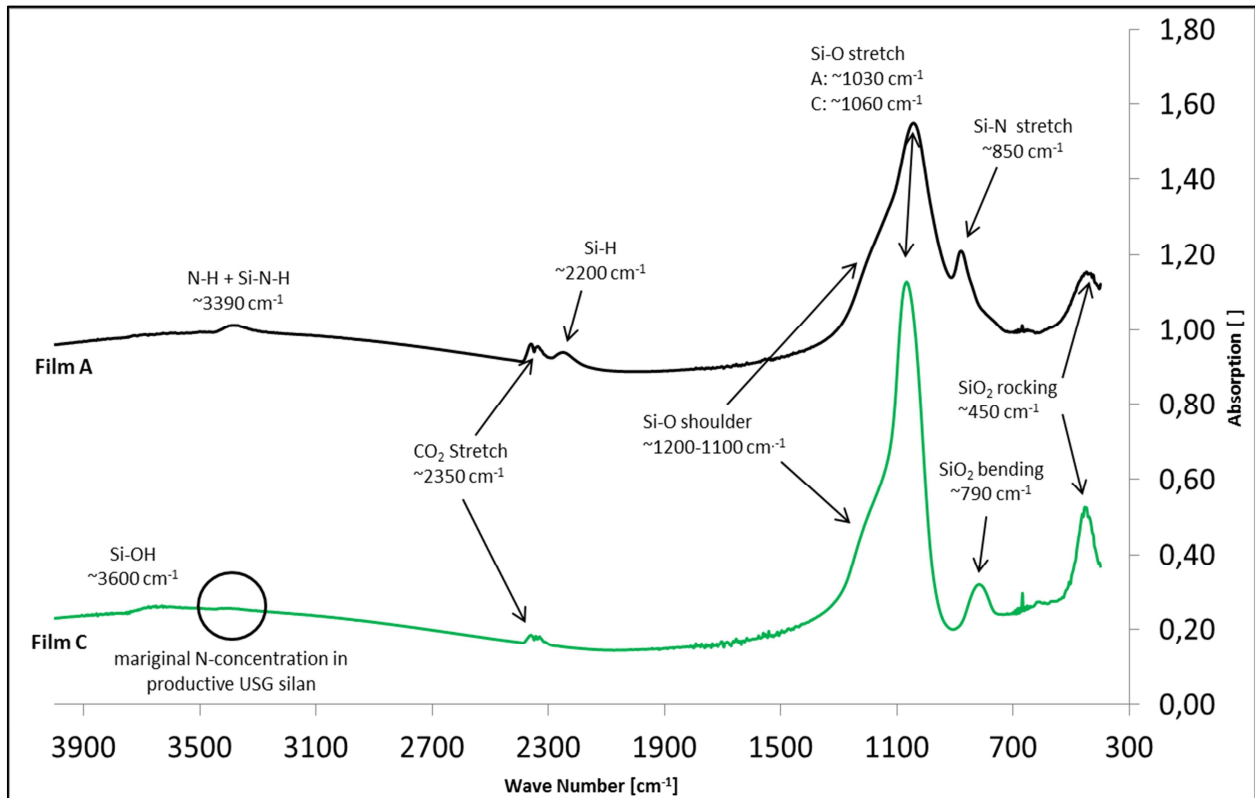


Figure 16: Comparison of the IR spectra between the nitrogen and hydrogen-rich USG film, Film A and the production USG film, Film C.

In connection with the infrared results above it can be stated that the chemical composition of Film A is $\text{SiO}_x\text{N}_y\text{H}_z$ where the subscripts x , y and z sum up to two ($x+y+z=2$) and the oxygen fraction is much greater than the nitrogen and hydrogen species in the dielectric film ($x \gg y, z$). The film systems B, C and D can be described as almost perfect USG films with a stoichiometric composition of SiO_xH_y . Subscripts x and y sum up to approximately two ($x+y \leq 2$) and x is significantly greater than y ($x \gg y$). The reason why the stoichiometric formula contains an OH group is due to a minor fraction of silanol (Si-OH) that is not completely condensed in the amorphous material, which can be seen as a small spectral band around 3600 cm^{-1} , as seen in Figure 16.

2.4. Surface Analysis

Since the main objective of the project is to investigate the cracking behaviour of USG silane films due to high nitrogen and hydrogen concentrations optical analysis was performed after deposition and wafer curvature experiments. Light microscopy is a powerful tool to investigate cracks and other surface damage. An Olympus optical light microscope was used to examine the surface of the dielectric films. To obtain detailed information of the surface topography and roughness properties all four film samples were investigated with an atomic force microscope (AFM) using silicon cantilevers with a tip radius of approximately 10 nm, for high lateral resolution. Before thermal treatment all of the films showed no surface cracks or damage as seen in Figure 17.

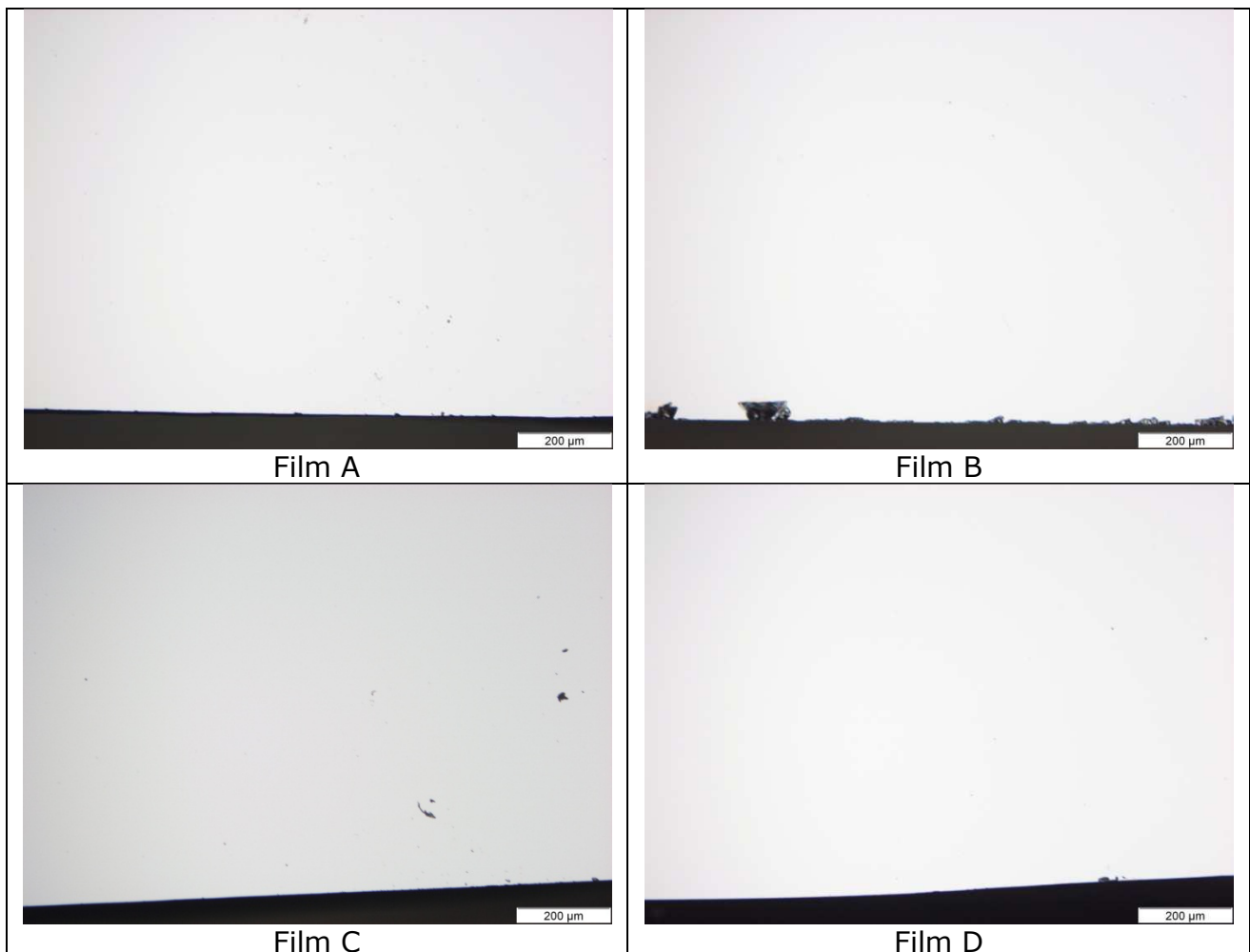


Figure 17: Light microscope images of Films A, B and C and D after deposition, indicating the crack-free surfaces.

To examine the surface roughness of the deposited films before and after heat treatment an AFM from Digital Instruments (Nanoscope Dimension 3100) was used. Since the amorphous films have no grain boundaries and the four USG films look very similar, a 3D image of Film C (productive USG film) is shown in Figure 18 below, to represent the surface of an amorphous dielectric material. To quantify the surface of the deposited films the Root Mean Squared (RMS) roughness and the absolute height difference were determined using the Nanoscope software. This statistical quantity can be defined as the deviation of the actual surface topography from an ideally smooth surface [33]. The RMS roughness is given by the standard deviation of the z-values (height values) for the sample area, as given by equation

$$R_{rms} = \sqrt{\sum_{n=1}^N \frac{(Z_n - Z_{av})^2}{N}} \quad (10)$$

where Z_n is the measured height Z_{av} the average height and N is the number of total height measurements. Table 4 summarises the RMS roughness results and the absolute height differences (Z_{abs}) of the surfaces of the four as-deposited film systems. By looking at Table 4 it can be seen that the surface roughness of the silane based (Film A, B and C) and the TEOS based (Film D) are different. Film D exhibits a much smoother surface with an absolute height difference of a few nanometers. The film systems A, B and C instead have significantly rougher surfaces.

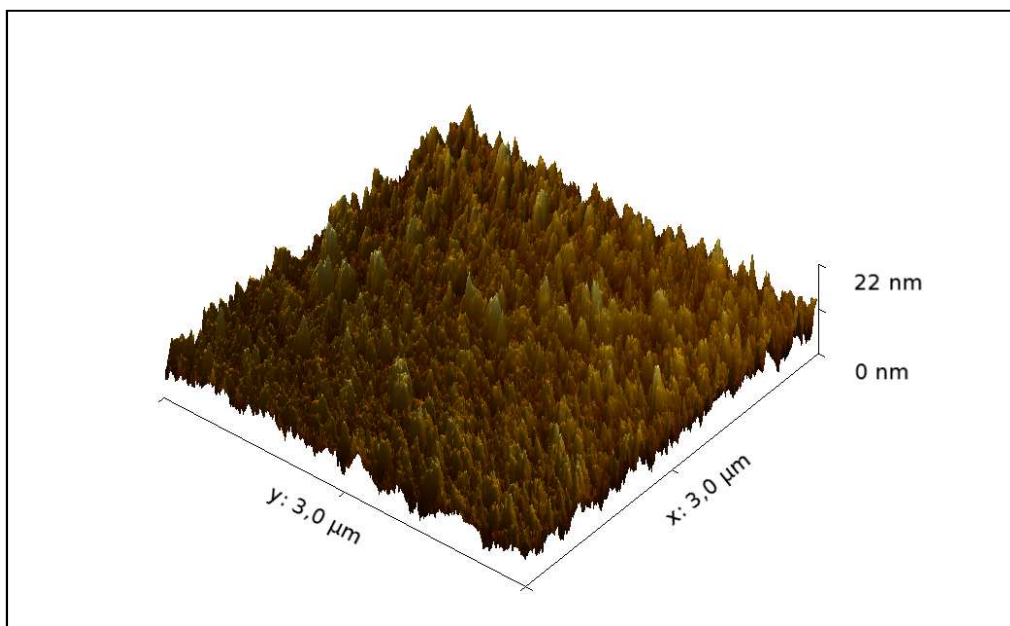


Figure 18: AFM 3-D height image of Film C showing representative surface roughness of amorphous silicon dioxide.

Table 4: RMS roughness and absolute height values of Film A, B, C in the as deposited state.

surface parameters: as deposited		
Film System	RMS [nm]	Z _{abs} [nm]
A (high H + N)	2.9	34.3
B (low H + N)	2.3	22.2
C (USG)	2.6	21.8
D (TEOS)	0.5	4.6

2.5. Mechanical properties of the as-deposited films

For the performed indentation measurements a Hysitron Triboscope nanoindenter with cube corner indenter was used. To determine the mechanical properties the Oliver and Pharr method was applied [34]. Loads from 1,000 to 10,000 μN were configured using 2 seconds for applying and unloading the load with a 10 second hold time at maximum load. The used cube corner indenter tips were calibrated using fused silica as the calibration material. From the load-displacement curves, the reduced elastic modulus and hardness were determined using a power law curve fit of the initial unloading curve and the corresponding area function.

Figure 19 shows the reduced elastic modulus results obtained for the four films. The reduced elastic modulus values should be converted into elastic modulus values from the film using,

$$\frac{1}{E_r} = \frac{(1-\nu_i^2)}{E_i} + \frac{(1-\nu_f^2)}{E_f} . \quad (11)$$

where ν_i is the Poisson's ratio of the diamond indenter, ν_f the Poisson's ratio of the film, and E_i and E_f the elastic modulus of the indenter and the film, respectively. For the deposited films a Poisson's ratio of 0.17 was chosen (see Table 1). In Figure 19 it can be seen that there is a linear dependence of the elastic modulus with the contact depth. This is due to the large difference in the elastic properties of the silicon substrate and amorphous SiO_2 film. There are numerical and also analytical models to deal with the influence of the substrate material. In order to compare the four films,

the elastic moduli are extrapolated to the contact depth of 0 nm [28]. Table 5 shows the extrapolated results.

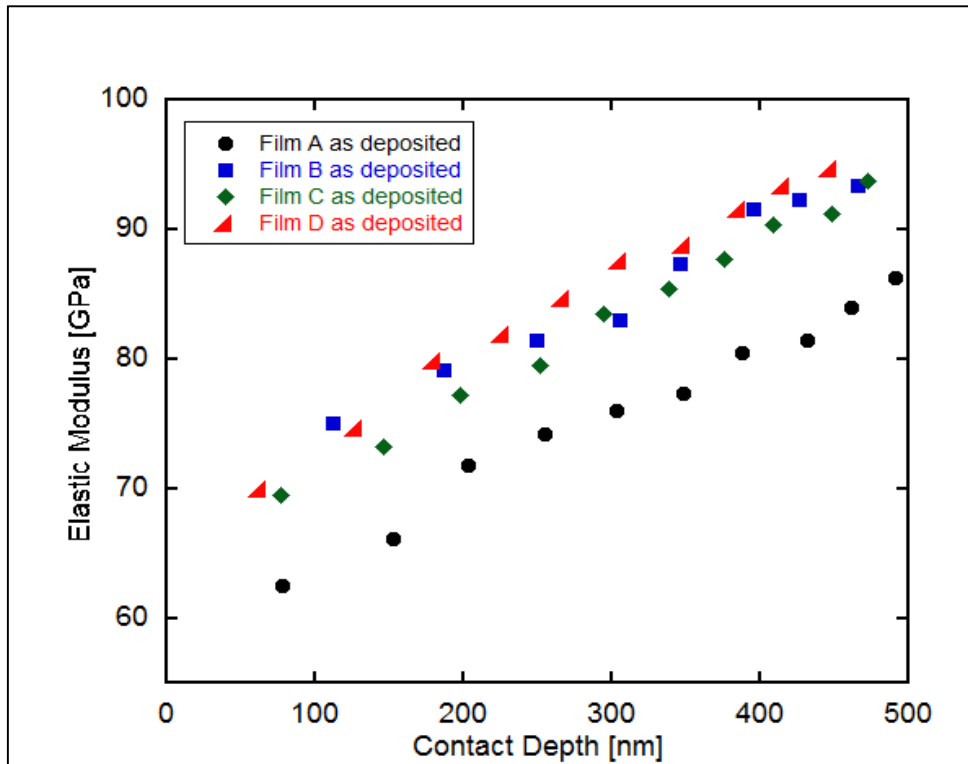


Figure 19: Elastic moduli of Films A, B, C and D after deposition. All films exhibit a linear behaviour with contact depth. Films B, C and D have similar elastic properties, while Film A has a lower elastic modulus.

Table 5: As deposited mechanical data of Films A, B, C and D.

Mechanical Properties: as deposited		
Film System	Elastic Modulus [GPa]	Hardness [GPa]
A (high H + N)	59.0	8.3
B (low H + N)	67.5	9.6
C (USG)	64.7	8.7
D (TEOS)	67.2	9.8

Comparing the results it is clearly shown that high concentration of hydrogen and nitrogen lead to a slightly lower elastic modulus. This can be explained by the lower network density of connected SiO₄ tetrahedrons and the large amount of uncondensed molecular species. Describing such an elastic material as a system of connected springs it is obvious that a higher percentage of disconnected springs will lead to a lower elastic modulus and a less stiff material.

Films B, C and D are approximately in the same range which supports the obtained results from the FTIR characterisation and the measurement of the refractive index. From Figure 19 it can be stated that the USG silane standard process film has an overall lower elastic modulus than the current standard USG TEOS based film (Film D). Nonetheless it is possible to improve the mechanical properties providing higher plasma power and a lower precursor gas flow. Therefore, Film B has approximately the same elastic modulus as the USG TEOS film (Film D).

The hardness values of the four deposited films are also shown in Table 5. The hardness was determined using the calculated contact depth from the power law curve fit divided by the maximum load. Hardness is a measure of how resistant solid matter is to permanent deformation when a force is applied. In the case of the deposited USG films on as (100) substrate, no depth dependent behaviour of the hardness was observed and the hardness of silicon and silica glass are in the same range [35].

As shown in Table 5, when Films A and C are compared to Films B and D, the two pairs have similar hardness values. It is interesting to see, that the current standard USG silane based film has a lower hardness than Films B and D, although it has very similar elastic properties.

3. Thermal Cycling to 1000°C

During wafer fabrication deposited dielectric PECVD films undergo an annealing process where temperatures reach up to 1050°C. This film heating process induces high thermal stresses because of the mismatch in thermal expansion coefficients between the film and the substrate. Internal stresses can arise when chemical changes occur. For example, the high concentration of nitrogen and hydrogen in USG films can lead to higher stresses at higher temperatures, and subsequently leads to material failure. Therefore, the dielectric films were characterised after thermal treatment to determine the effects of such annealing processes.

3.1. Wafer Curvature Experiments

To get a deeper insight into what is happening during thermal processes, wafer curvature is an excellent non-destructive in-situ method to measure thin film stress. It is very important to verify that measurement conditions are comparable to industrial temperature processes in the wafer fabrication facility. Therefore, the instrument specification of the wafer curvature device has to meet the high temperature requirements of such a process.

The measurement system shown in the Figure 20 was build using a new vacuum chamber and heating system to enable high temperature wafer curvature measurements up to 1000°C. A 3.5 kW Boron-nitride heating plate was used, where the temperature was measured by a thermal element integrated into the ceramic heating plate. The temperature was controlled by an electric relay connected to the measurement software. Adjustment of the laser optics was performed so that no geometric effects coming from the wafer curvature setup occurred. Measurements were all performed under vacuum conditions in the pressure region of approximately 10^{-4} mbar.

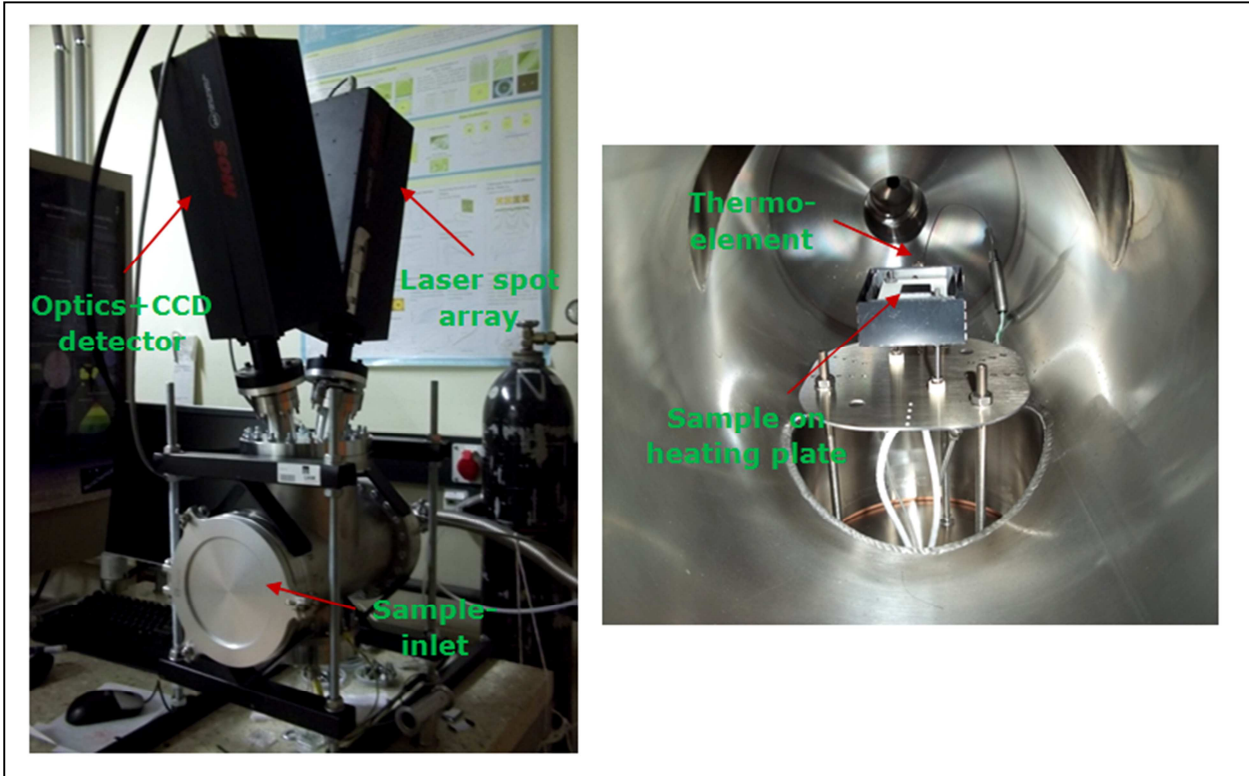


Figure 20: Wafer curvature system for high temperature measurements. Left image shows the setup of the measurement device. Right image displays the heating plate and the built-in thermo-element for temperature control.

In terms of the experimental procedure all materials were thermally cycled using a 20K/min heating and cooling rate. One thermal cycle consists of heating the sample up to 1000°C from room temperature and then was cooled down (no holding time at 1000°C) to 70-60°C. Cooling rate of 20K/min was achieved down to temperatures of ~135°C and then to the rate decreases since cooling in vacuum can be a very slow process. Additionally, the coefficient of thermal expansion was determined using the slope of the stress temperature curve in the cooling cycle between 300°C and 150°C. The thin film mean CTE can be extracted from the wafer curvature data using the formula

$$\alpha_f = \alpha_s - \frac{1}{E_s} \frac{d\sigma_f}{dT}. \quad (12)$$

The CTE of the film, α_f , is calculated using the mean expansion coefficient α_s of silicon between 300°C and 150°C, the biaxial modulus E_s of silicon and the slope of the stress temperature curve in the chosen temperature range. The values used for biaxial modulus and the mean CTE of silicon were 180 GPa and 3.5 ppm/°C [36], [37].

At this stage it should be mentioned that the temperature is always referred to the heating plate temperature. This approach is also applied in rapid thermal annealing processes in production since it is a very crucial topic to measure sample surface temperatures regardless whether it is contact temperature measurement (thermocouple) or non-contact measurements (pyrometer).[38],[39]. Thus, when the film thickness is much smaller than substrate thickness it can be assumed that ($h_f \ll h_s$) and no temperature gradient is present in the film.

Looking at Figure 21 one can see the thermal cycle of the four different film systems. Films B, C, and D exhibit similar thermomechanical behaviour which can be described as thermoelastic behaviour since there are no massive irreversible stress changes present after one thermal cycle. Therefore, the stress contributions are only generated by thermal expansion mismatch properties between the substrate and film material.

This can be also seen in Table 6 by comparing the absolute stress difference (stress difference between room temperature and 1000°C from the heating cycle) and the CTEs of Films B, C and D. All of the films have a CTE of about 2.5ppm/°C and an absolute stress difference of about 600 MPa. This suggests that the three films illustrate the thermomechanical behaviour of almost perfectly stoichiometric SiO₂ glass films. In contrast, the high concentrations of hydrogen and nitrogen species lead to massive stress evolution like seen in Film A.

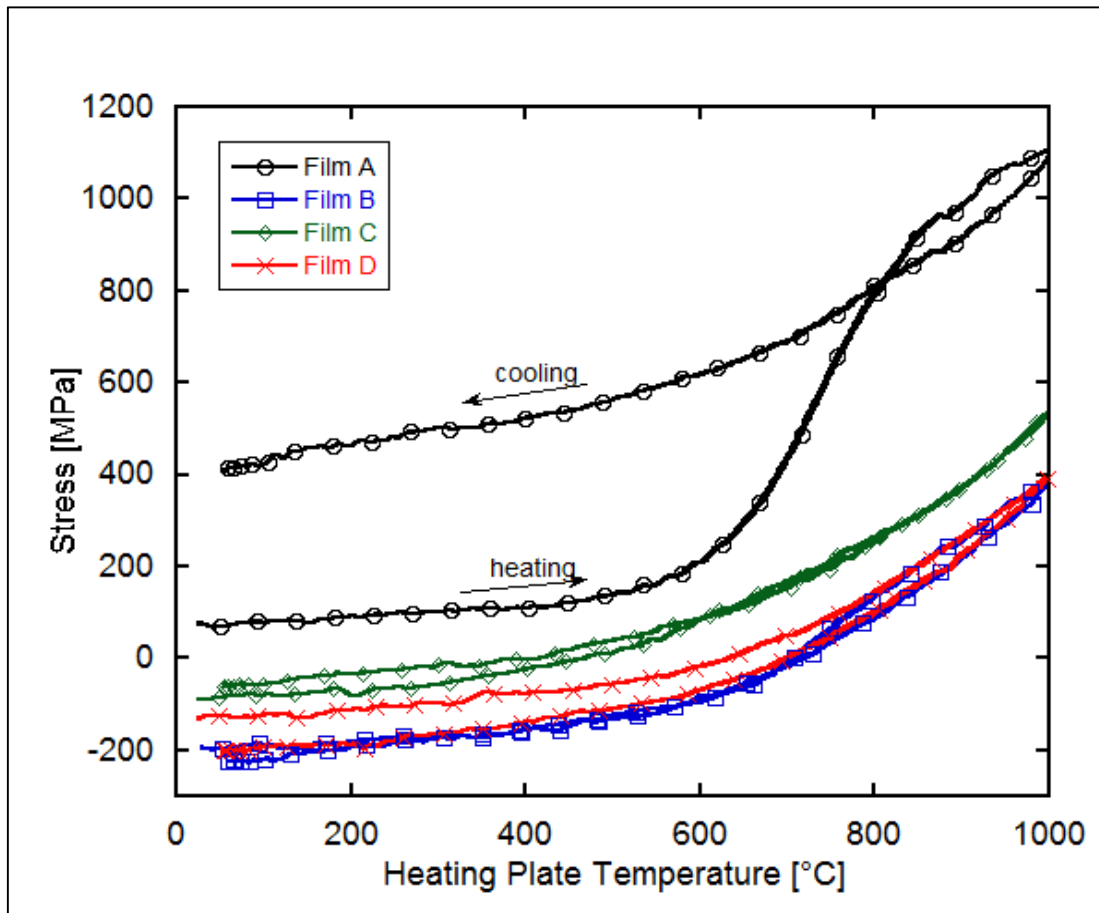


Figure 21: Stress-Temperature cycles of Films A, B, C and D. The thermomechanical behaviour of Films A, B and C can be described as completely thermoelastic, in contrast to Film B which shows large irreversible stress changes due to hydrogen and nitrogen species.

Figure 22 shows the stress-temperature curve of Film A compared to the optimised USG film, Film B. Somewhere around 550°C stress differences can be seen. Assuming that Film B has almost no chemical impurities or trapped species in the glass network, the evolved stress differences at higher temperatures in Film A can be attributed to the remaining nitrogen and hydrogen species after deposition. These chemical impurities lead to chemical changes in the film material and to additional tensile stresses. Therefore, an overall stress difference of about 1025 MPa can be seen which resulted in an irreversible stress change of about 360 MPa after one thermal cycle. The mean CTE of Film A was calculated to be 1.9 ppm/K which is slightly lower than the other three films which could arise from the chemical changes during the thermal cycle. It should be mentioned that the thermal expansion coefficients of the four films differ from the bulk value (0.55 ppm/K see Table 1). This would indicate that in thin films the thermal properties differentiate from their bulk equivalents.

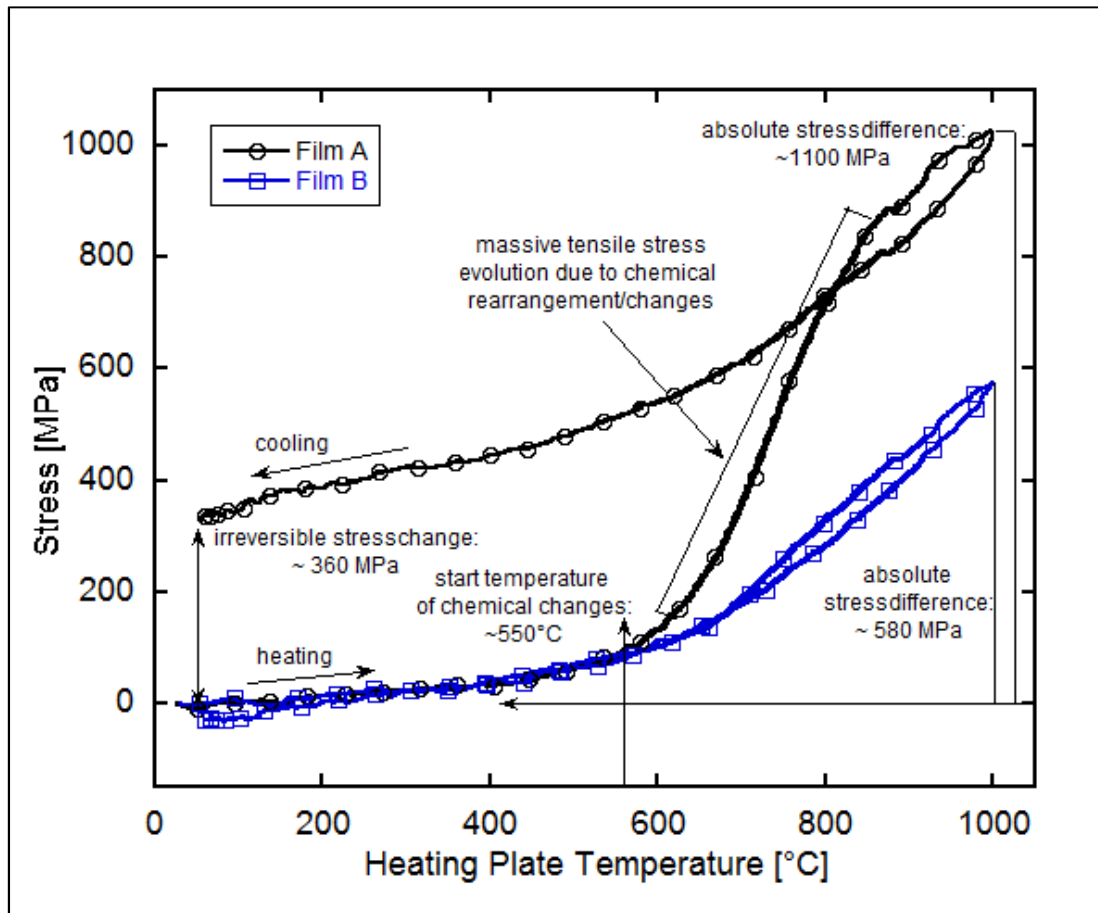


Figure 22: Comparison between Film A (high Nitrogen + Hydrogen content) and Film B (optimised USG film) wafer curvature curves. Massive stress evolution starting around 550°C in Film A can be observed.

Table 6: Summary of the wafer curvature results of Films A, B, C and D.

Wafer Curvature Results			
Film-System	Coefficient of Thermal Expansion [$\times 10^{-6}/^{\circ}\text{C}$]	Irreversible Stress Change [MPa]	Absolute Stress Difference [MPa]
A (high H + N)	1.90	360	1025
B (low H + N)	2.40	0	610
C (USG)	2.54	0	625
D (TEOS)	2.59	-70	600

3.2. FT-IR

Figure 23 displays the FT-IR spectra of the four different film systems after one thermal cycle. The spectra of Films B, C and D remain almost identical compared to the as-deposited spectra. The only chemical change can be assigned to the disappearance of the broad Silanol (Si-OH) around 3600 cm^{-1} . This suggests that the heat treatment led to complete condensation of Si-O-Si bonds and would indicate that after heat treatment Films B, C and D have a chemical composition of SiO_x , where index x is very close to two ($x \leq 2$, resulting in stoichiometric SiO_2).

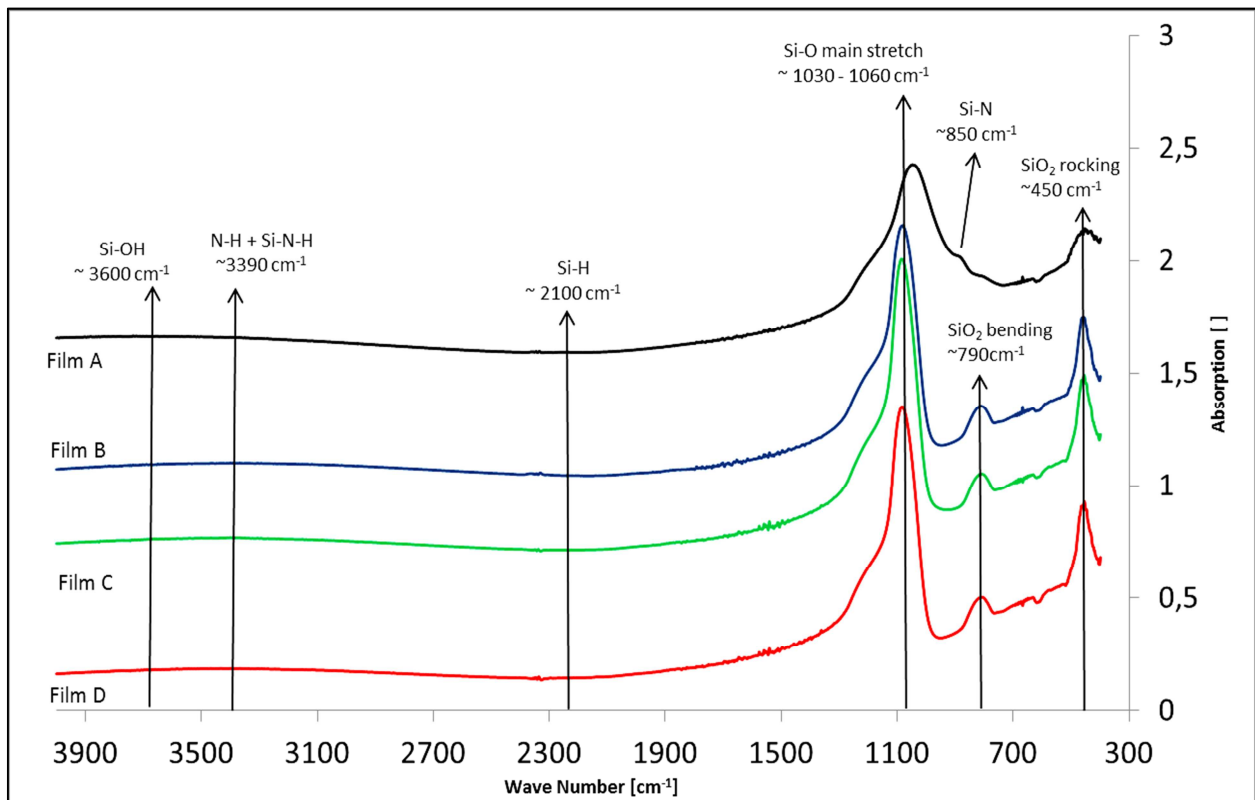


Figure 23: FT-IR spectra of Films A, B, C and D after one thermal cycle. Disappearance of Si-H and Si-N-H band and peak reduction around $900\text{-}700\text{ cm}^{-1}$ in Film A. Spectra of Films B, C and D remain more or less unchanged after heat treatment, except for the disappearance of the small Si-OH band

The spectrum of Film A shows significant changes after one thermal cycle. The N-H band around 3390 cm^{-1} completely vanished, suggesting that no N-H bonding is present after heat treatment. The Si-H peak around 2100 cm^{-1} has also almost completely vanished. In the spectral region of $900\text{-}700\text{ cm}^{-1}$ the peak size was reduced by a reduction of hydrogen and has led to more defined peaks. Film A also exhibits a small Si-N band at around 850 cm^{-1} and at around 790 cm^{-1} a small SiO_2 bending peak is now observed. Both of these peaks are overlapped by the large broad

Si-O main stretch peak. By combining the infrared results in the next section, it can be stated that the chemical composition of Film A is **SiO_xN_yH_z** where the subscripts x y and z sum up near to two ($x+y+z \leq 2$) and the Oxygen fraction is much greater than the nitrogen and hydrogen species are only present in a minor fraction ($x \gg y > z$).

3.3. Surface Characterisation

The thermally cycled samples were investigated with a light microscope at various magnifications. Cracks were found on Film A, which are displayed in Figure 24. The cracks run through the sample in parallel arrays. Film B, C and D did not exhibit any cracking and remain unchanged in terms of their optical appearance.

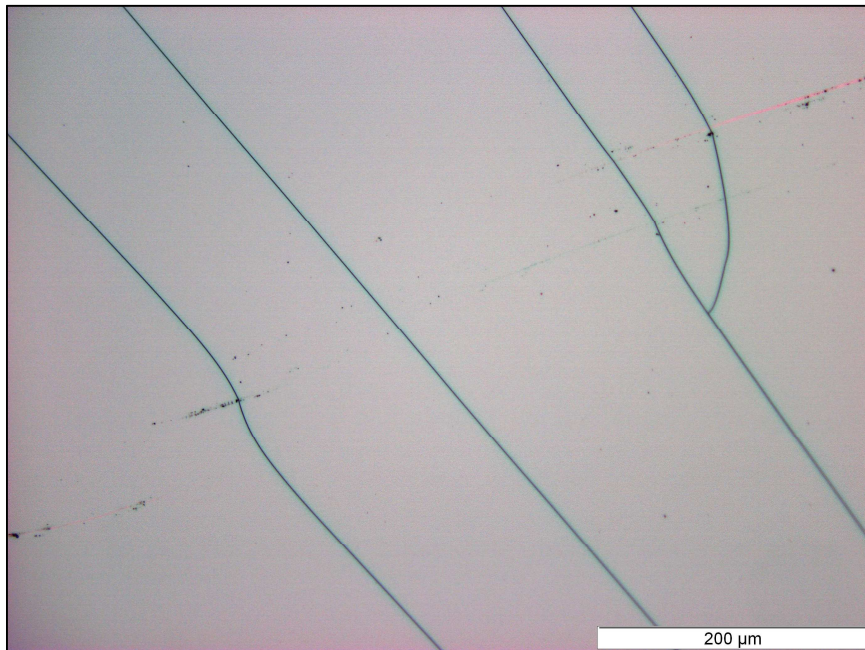


Figure 24: Optical image of Film A illustrating the parallel crack arrays found after thermal cycling.

As stated in Section 2.4, the four film systems were investigated in terms of their surface properties after one thermal cycle. Table 7 displays the roughness results from the Nanoscope software. Compared with the as-deposited results from Table 5 no change in terms of the surface roughness can be seen. RMS and the absolute height difference remain unchanged before and after heat treatment. This would suggest that up to temperatures of 1000°C no significant surface diffusion is present.

Table 7: RMS roughness and absolute height values of Film A, B, C and D after one thermal cycle.

surface parameters: after thermocycle		
Film System	RMS [nm]	Z _{abs} [nm]
A (high H + N)	2.4	19.9
B (low H + N)	2.7	27.0
C (USG)	2.3	19.2
D (TEOS)	0.5	4.8

3.4. Nanoindentation

The measurements of the annealed samples were performed in the same way as described in Section 2.5. Figure 25 displays the depth dependent elastic modulus of the four different film systems. The open symbols show the as-deposited values compared to the closed symbols, which display the thermal cycled measurements. The elastic modulus of Films B, C and D is slightly higher after one complete thermal cycle, but overall remains the same. This also matches with the chemical data obtained by infrared spectroscopy. Therefore only the broad Si-OH band disappeared which implies a further condensation of Si-O-Si bonds but only in a very small quantity.

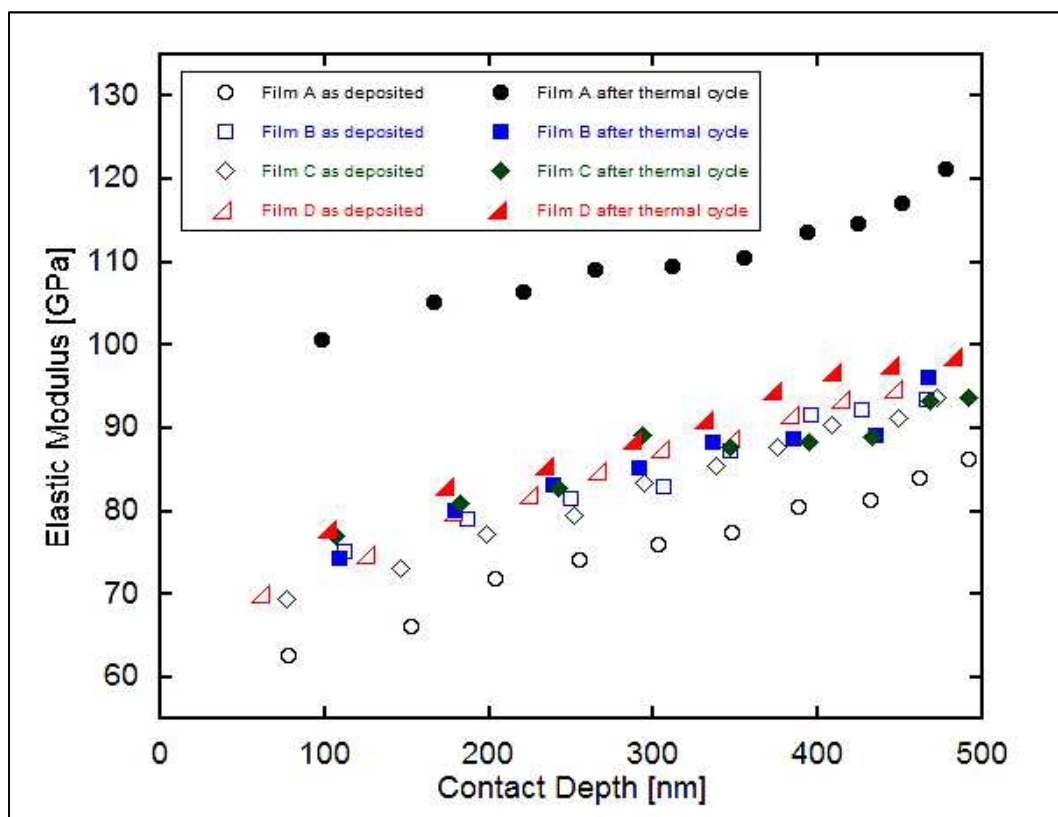


Figure 25: Comparison of the elastic moduli before and after a complete thermal cycle of Films A, B, C and D. Films B, C and D remain approximately unchanged in terms of their elastic properties, whereas Film A shows a large increase due to chemical changes indicated by the FT-IR data.

The elastic modulus and hardness values of Film A increased about 38% after one complete thermal cycle compared to the as deposited sample. The nitrogen species leads to partial Si-N bonding in the glassy network, which results in a stiffer structure and a higher elastic modulus. In other words a high nitrogen concentration leads to nitrogen doped silicon dioxide which is called a silicon oxynitride (SiO_xN_y). When looking at the mechanical data of Films B, C and D no significant mechanical property

change can be observed. This is due to the almost perfect SiO₂ composition and no presence of nitrogen in the glass network. Table 8 gives the extrapolated elastic moduli (modulus at contact depth 0 nm) and the hardness values.

Table 8: Summary of the mechanical properties of the as deposited and after one thermocycle of Films, A, B, C and D.

Mechanical Properties				
Film System	<i>as deposited</i>		<i>after thermal cycle</i>	
	Elastic Modulus [GPa]	Hardness [GPa]	Elastic Modulus [GPa]	Hardness [GPa]
A (high H + N)	59.0	8.3	96.1	11.1
B (low H + N)	67.5	9.6	69.9	9.7
C (USG)	64.7	8.7	73.7	9.6
D (TEOS)	67.2	9.8	72.5	10.1

Both, the elastic modulus and the hardness values show the difference between the stoichiometric silicon dioxide films (Films B, C and D) and the nitrogen doped Film A. All SiO₂ like films exhibit approximately the same elastic modulus as the bulk material fused silica, which is about 70. GPa [40]. The hardness after one thermal cycle for Films B, C and D is on the same order which supports the obtained elastic material properties. Similar to the elastic modulus, the hardness of Film A increased significantly after heat treatment compared to the as-deposited hardness.

4. Temperature resolved experiments of Film A

With the results from Chapter 3 the question regarding Film A arose: what exactly occurs during the thermal cycle. For that reason an experimental method was developed to get a better understanding when mechanical and chemical changes appear. Using the stress-temperature curve of Film A (Figure 22), one can clearly see when massive stress changes start. Therefore, different peak temperatures were chosen to get further information on what occurs between room temperature and 1000°C. Figure 22 shows that significant stress changes develop around 550°C. Below that temperature a linear stress response can be observed which is due to thermal expansion mismatch between film and silicon substrate. Additional peak temperatures of 500, 600, 700, 800 and 900°C were chosen to obtain a temperature resolved analysis of Film A. Additional samples were treated the same way as in the previous wafer curvature experiments (same heating and cooling rate), except that the maximum temperatures of the thermal cycles were changed with the temperature values mentioned above. Subsequently, each thermally cycled sample was analysed using FT-IR, light microscopy, and nanoindentation.

In Figure 26 the six thermal cycles to different peak temperatures are shown. An irreversible stress change develops with peak temperatures greater than 500°C supporting the assumption that chemical changes in the dielectric film start at temperatures between 500 and 600°C. From the figure it can be seen that for the thermal cycle to 700°C peak temperature, the chemical changes also occur in the cooling segment. Thereby, the stress is also increasing from 700°C down to 650°C in the cooling segment. This phenomenon cannot be seen at peak temperatures of 900°C and 1000°C which would suggest that there is no further chemical stress evolution. Interestingly, thermal cycles with 800 and 900°C peak temperatures show a higher irreversible stress change than the 1000°C sample. Results of the thermally resolved stress evolution (Table 9) provide the linear thermal expansion coefficient of Film A determined between 300°C and 150°C in the cooling segment.

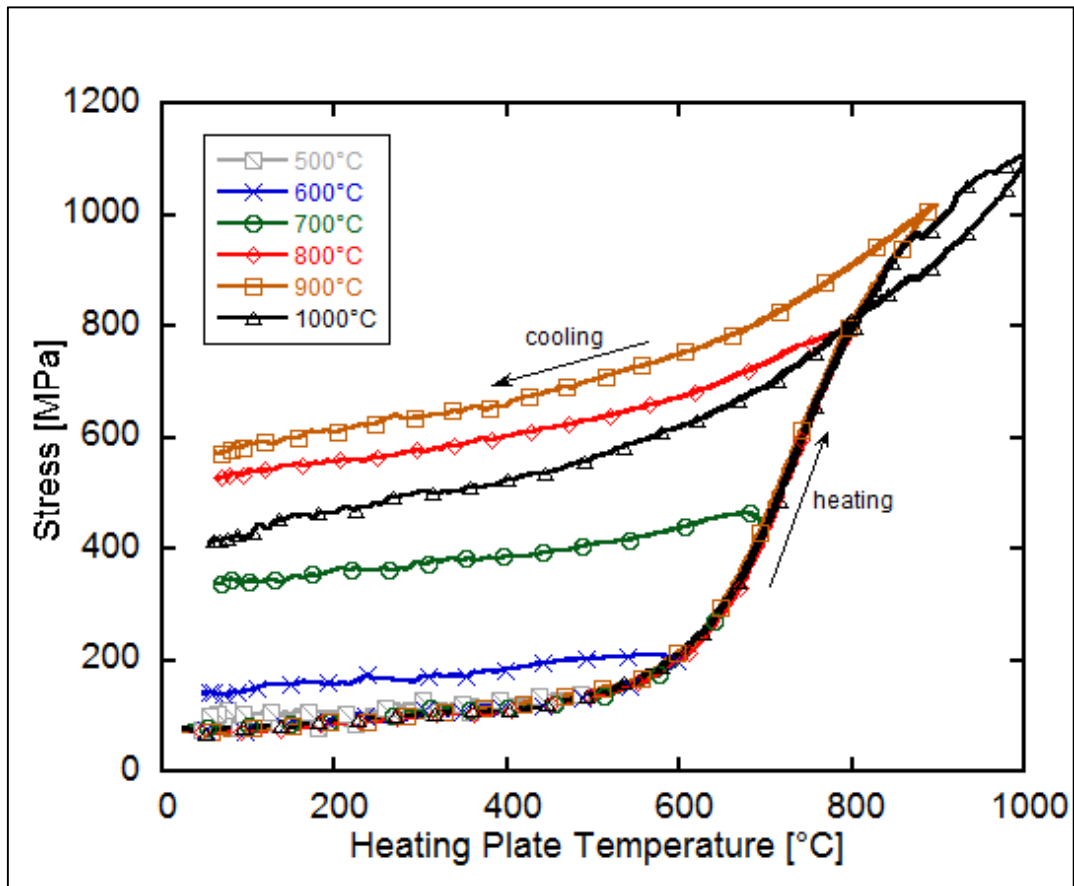


Figure 26: Wafer curvature heat cycles with different peak temperatures. Up to 500°C no irreversible stress generation can be observed. Higher peak temperatures lead to large stress changes.

Table 9: Thermally resolved stress-temperature data of Film A.

thermal resolved Wafer Curvature Data of Film A (high H + N)			
Peak-Temperature [°C]	Coefficient of Thermal Expansion [$\times 10^{-6}/^{\circ}\text{C}$]	Irreversible Stress Change [MPa]	Absolute Stress Difference [MPa]
500	2.55	30	70
600	3.10	70	130
700	2.53	270	350
800	2.55	460	720
900	2.16	500	930
1000	1.91	350	1030

After wafer curvature experiments the thermally cycled films were investigated in terms of crack formation using the optical microscope. Cracks appear on samples with a peak temperature of 800, 900 and 1000°C, indicating that high nitrogen and

hydrogen concentrations lead to crack formation far before peak temperatures of common thermal treatments (e.g. 1050°C). This implies that the tensile fracture stress for Film A was between 430 MPa and 780 MPa by looking at the stress temperature data.

The thermally cycled samples with different peak temperatures were then analysed using FT-IR. Figure 27 gives the chemical evolution of Film A from room temperature up to 1000°C. The important peaks, which are most influenced by the heat treatment are indicated with straight lines. It can be seen that up to peak temperatures of 700°C the spectra look more or less the same, suggesting that no bond cleavage (bond re-arrangement) appears. From 800 to 1000°C peak temperature, the N-H band around 3390 cm^{-1} completely vanishes along with the Si-H peak. This implies that temperatures greater than 700°C are needed for hydrogen cleavage from nitrogen and silicon. At the same temperature range the overlapped Si-N peak at 850 cm^{-1} wave numbers change due to the cleavage of hydrogen and the condensation of nitrogen with silicon. The significant reduction of Si-H bonds leads also to the detection of the SiO₂ bending vibrations around 790-780 cm^{-1} . The FT-IR spectra at a peak temperature of 1000°C shows a small, but defined SiO₂ bending peak next to the Si-N peak. Both peaks are overlapped by the main Si-O stretch at 1030 cm^{-1} .

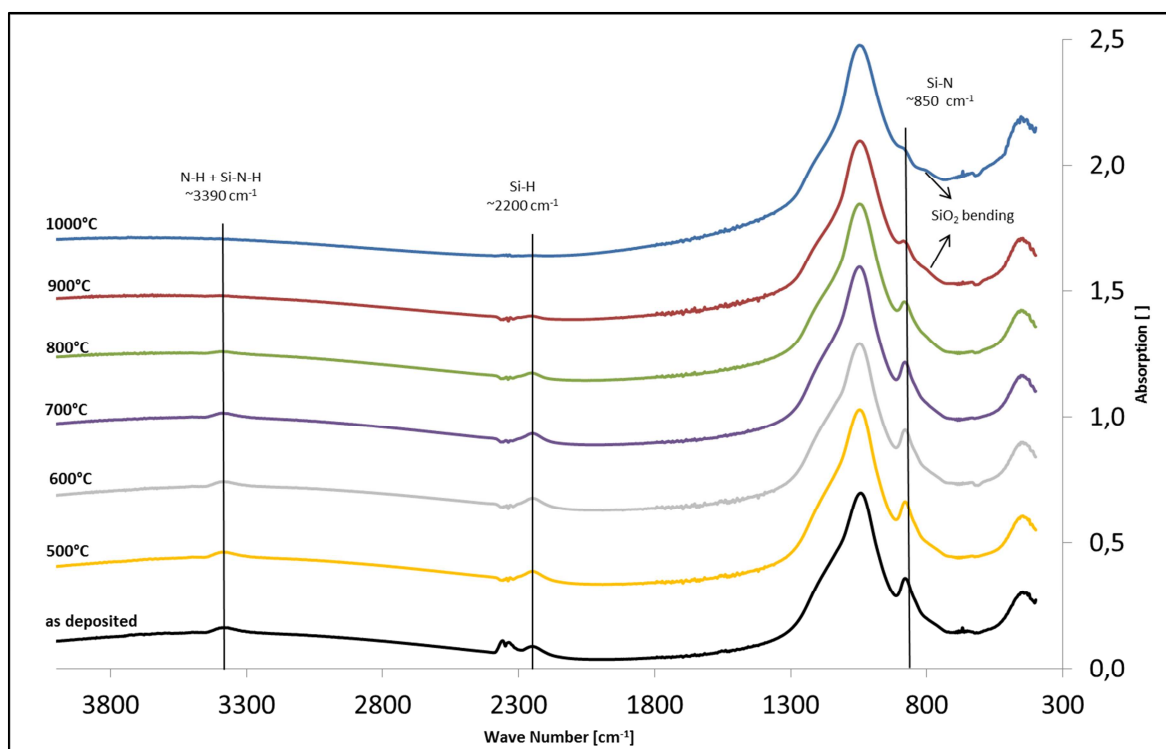


Figure 27: Chemical evolution of Film A with different peak temperatures. Bond cleaves of Hydrogen occurs between temperatures of 700°C and 1000°C.

After non-destructive testing all thermally cycled samples to different peak temperatures were investigated in terms of the mechanical changes during a complete thermal cycle. All thermally cycled samples were indented with a cube corner tip using an applied load of 5,000 μN . For each sample five indents were made and the average value was calculated. Figure 28 and 29 display the changes of elastic modulus and hardness during a complete thermal cycle up to 1000°C heating plate temperature. Both mechanical data sets show that a significant increase of elastic modulus and hardness between temperatures of 500 and 1000°C. This was also found in the wafer curvature stress-temperature data in terms of the stress change. The significant stress change starting around 550°C matches with the mechanical property changes.

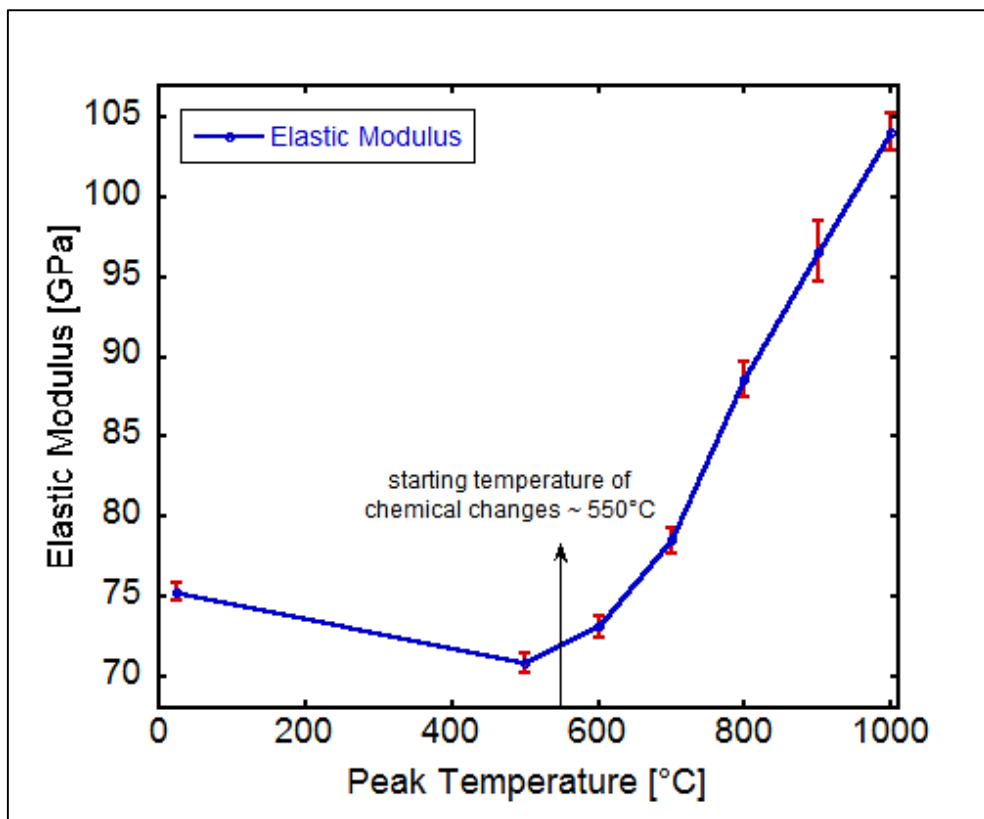


Figure 28: Thermally resolved elastic properties of Film A which display a large increase of the elastic modulus starting around 550°C.

As previously mentioned, the elastic modulus and hardness values of Film A increased about 38% after one complete thermal cycle compared to the as-deposited sample. In Film A, high nitrogen incorporation leads to doping of the SiO_4 tetrahedrons and therefore the bonding characteristics in the glass network. As shown in the thermally resolved elastic modulus and hardness plots, a strong increase of the mechanical properties starts with temperatures greater than 700°C. The shape of the thermally resolved elastic modulus and hardness plots suggests that there could be a further

increase at temperatures higher than 1000°C. Hence, structural network changes in terms of further condensation process of tetrahedrons are not completed after one thermal cycle.

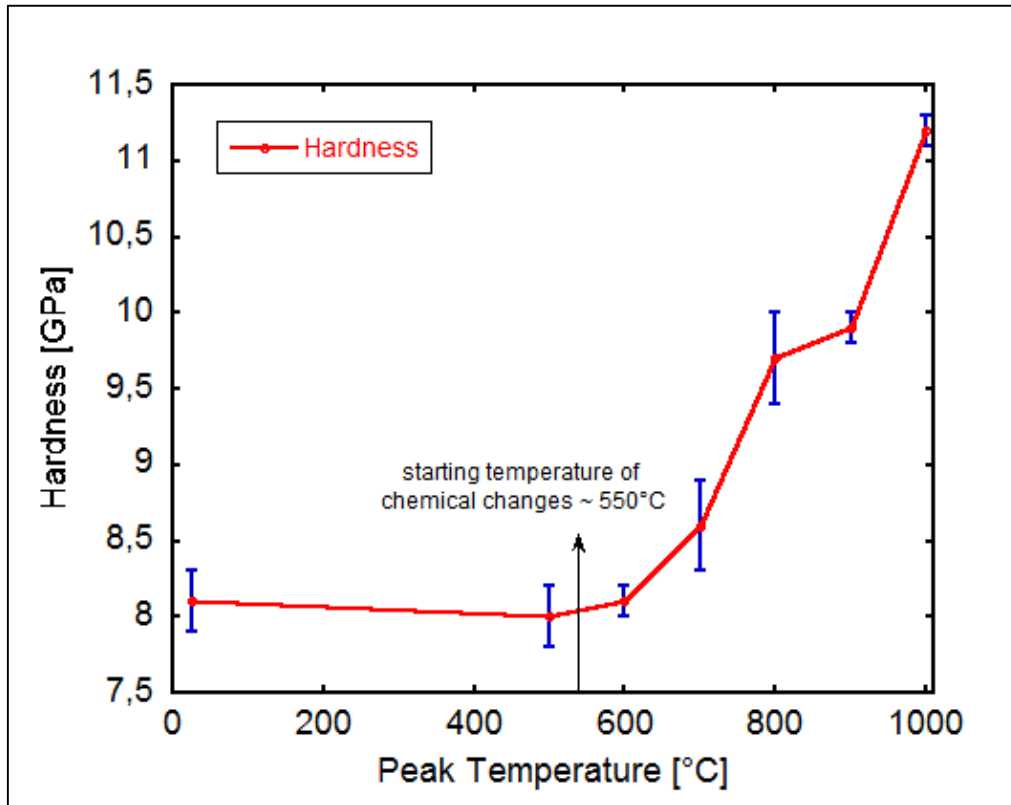


Figure 29: Thermal resolved hardness data of Film A, which displays a large increase at temperatures greater than 550°C.

To verify the laboratory experiments, the rapid thermal annealing process at the production plant in Villach was modified to provide the same heating and cooling rates (20 K/min) which were used in the wafer curvature experiments. This made it possible to thermally resolve a thermocycle in terms of the film thickness and the refractive index, where it was possible to measure the film thickness and the refractive index of Film A at different peak temperatures using the in-line ellipsometer. Figure 30 shows the film thickness evolution up to 1000°C peak temperature. Here it can be clearly seen that significant film thickness decrease starts between 500° and 600°C. This temperature area matches with the wafer curvature and the mechanical property results very well.

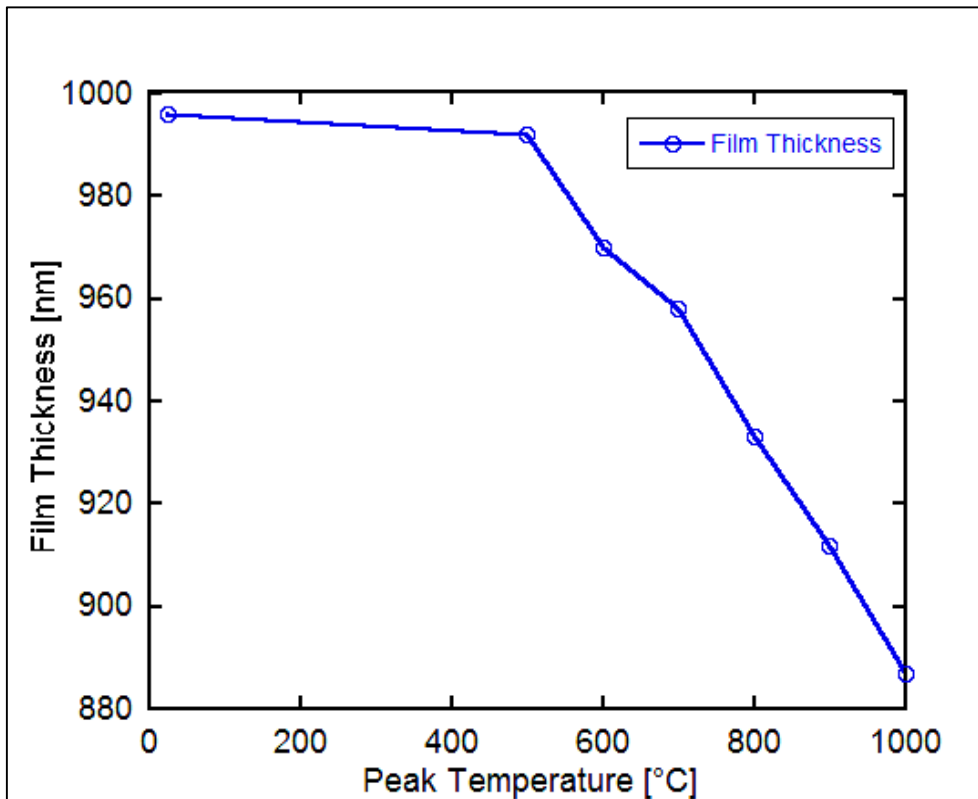


Figure 30: Thermal resolved film thickness of Film A. At peak temperatures between 500°C and 600°C the film thickness starts to decrease which results in a thickness loss of about 11% after one thermal cycle.

At a peak temperature of 500°C, Film A has only lost 0.4% of its thickness, which indicates that below those temperatures no chemical changes in the film system occur. From the temperature range between 500°C and 1000°C the shrinkage of the film thickness shows a linear behaviour. After a complete thermal cycle with a peak temperature of 1000°C the Film A loses almost 11% of its thickness. It also has to be mentioned that due to the steady film thickness decrease further shrinkage could occur at temperatures greater than 1000°C.

In terms of the optical changes with different peak temperatures Figure 31 shows the thermal resolved refractive index. During the thermal cycle the refractive index increases at temperatures greater than 800°C. Below that temperature there is a decrease between temperatures of 500 and 600°C.

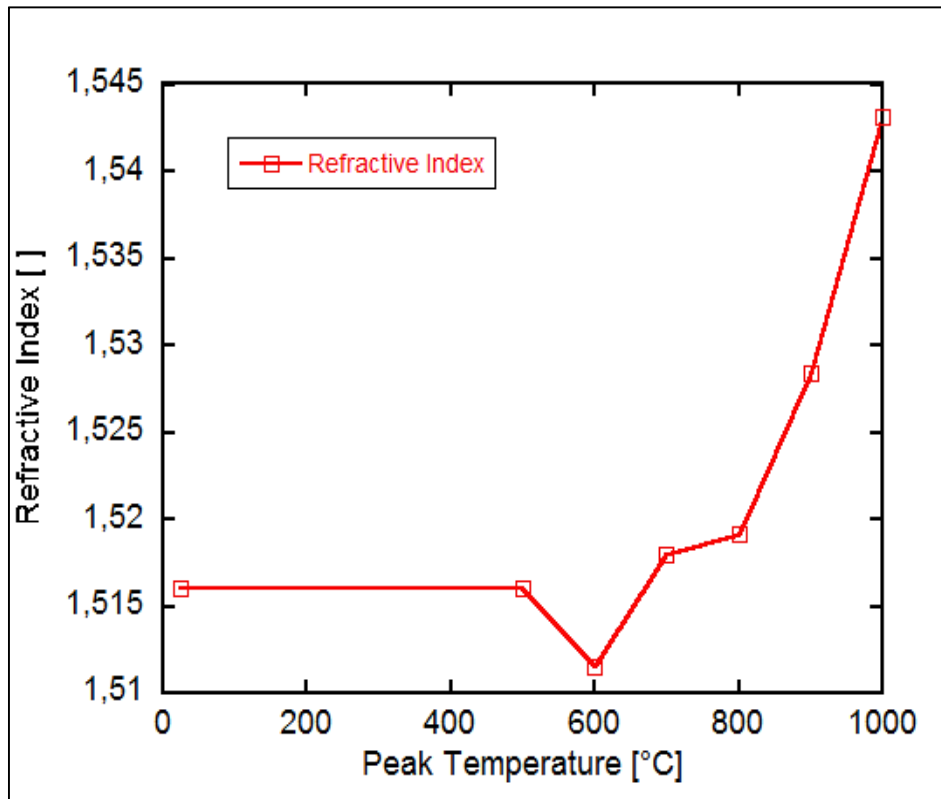


Figure 31: Thermal resolved optical properties of Film A. The refractive index increases significantly with temperatures greater than 800°C.

Differentiation of Nitrogen and Hydrogen Influence

Taking the conclusions from the previous experiments the final step was to subdivide the influences of nitrogen and hydrogen species in a silicon dioxide film. Therefore, two additional deposition recipes were developed which separate Film A into two independent film systems.

The high silane (SiH_4) and the additional nitrogen supply (NH_3) were separated into two independent deposition processes. Table 10 above shows the deposition parameters and for the new film systems, Films E and F compared to Film A. These new films were submitted to the same thermal treatment as Films A, B, C and D before to determine if nitrogen or hydrogen is has the higher impact in terms of the stress behaviour of USG films.

Table 10: Deposition parameters and initial properties of Film E and F compared to the high N and H containing Film A

deposition parameters							
Film-System	Heater-Temp. [°C]	Pressure [Torr]	N ₂ O [sccm]	SiH ₄ [sccm]	NH ₃ [sccm]	Spacing [mils]	RF [W]
A	400	2.7	3900	320	100	430	200
E				200	100	430	200
F				320	0	430	200
initial properties							
Film-System	Deposition Time [s]	Thickness [nm]	Dep. Rate [nm/s]	Range [nm]	Uniformity [%]	RI [-]	Stress [Mpa]
A	49	988	20.16	10	0.51	1.5182	72
E	64	1010	15.78	18	0.89	1.4839	17
F	48	1006	20.96	10	0.50	1.5082	40

Figure 32 shows the comparison of Films A, E and F in terms of their thermomechanical behaviour during one thermal cycle. Recall that Film A is the deposition process with high concentration of nitrogen and hydrogen species, whereas Film E has a high amount of remaining nitrogen species and Film F contains high amounts of hydrogen species. Film A and F reveal similar thermomechanical behaviour. Both have significant stress evolution starting between 500 and 600°C, where Film A has a slightly higher stress increase and total irreversible stress change. After thermal cycling Film F exhibited cracks but in a very small quantity compared to Film A, which can be seen in Figure 33.

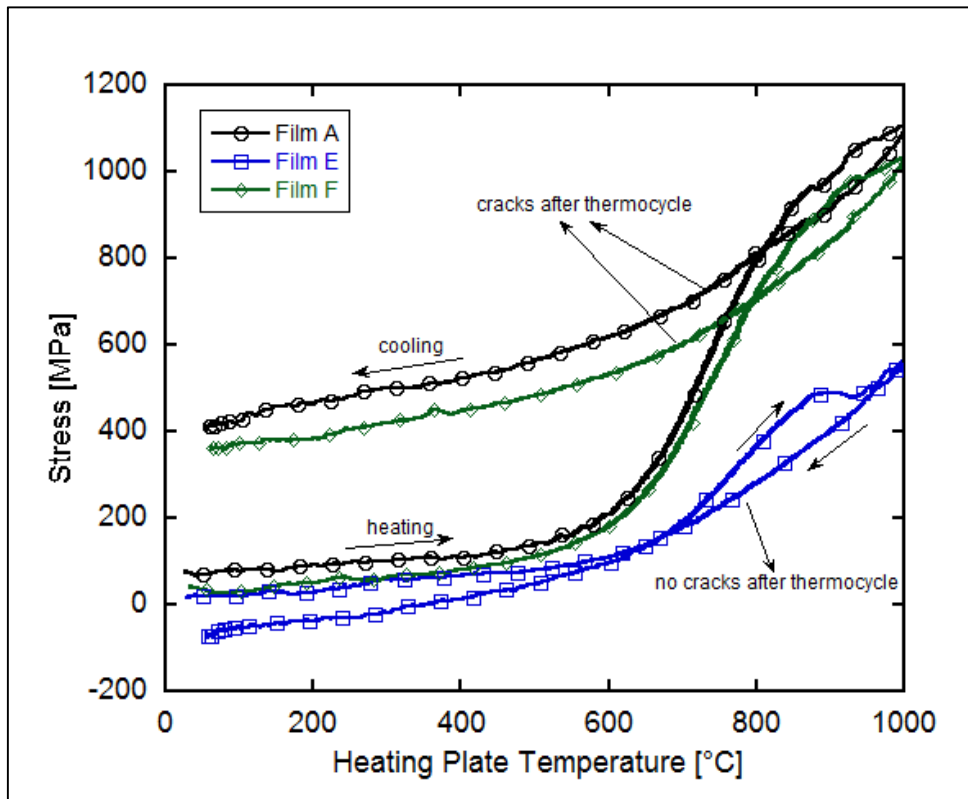


Figure 32: Stress evolution of an high N film (Film E) and a high H film (Film F) compared to Film A with a high N and H concentration

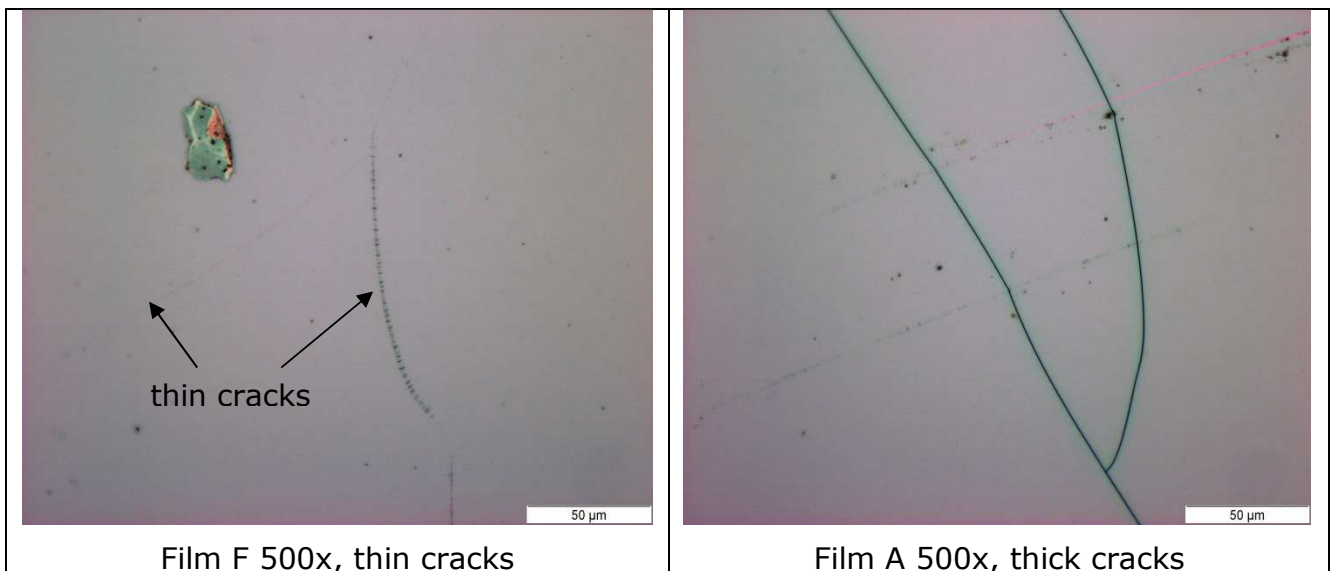


Figure 33: Light microscopy images of Film A and F. Film F revealed only a few cracks which were thin compared to Film A.

Film E, however, exhibits different thermomechanical behaviour. This dielectric film has a linear stress behaviour up to a temperature around 600°C and then a lower stress increase. At approximately 900°C there is a flat stress plateau followed by a

stress increase induced by thermal mismatch. The absolute stress difference of Film E with 520 MPa (in the thermal cycle) was smaller compared to Film B, C and D which showed a stress difference of approximately 600 MPa. This can be contributed to the relaxation stress plateau around 900°C.

Table 11: Stress-Temperature Data of Films A, E and F.

Wafer Curvature Film E and Film F			
Film-System	Coefficient of Thermal Expansion [$\times 10^{-6}/^{\circ}\text{C}$]	Irreversible Stress Change [MPa]	Absolute Stress Difference [MPa]
A (high H + N)	1.90	360	1025
E (H + high N)	2.55	-80	520
F (high H + N)	1.90	320	960

5. Discussion

In order to understand the influence of nitrogen and hydrogen impurities it is important to combine the obtained results from Sections 2 through 4. Therefore, the development of such a qualitative model of what happens during a heat treatment cycle in terms of stress behaviour, chemical composition, mechanical and optical properties, has to include all the collected results from the previous sections.

In terms of any sources of chemical impurities in deposited thin films one has to always remember that the origin is always the deposition process itself. All the as-deposited properties of the USG films are only controlled by the chosen deposition process and hence the used deposition parameters. By looking at Tables 2 and 3 one can see the chosen deposition parameters and the as-deposited results of Films A, B, C and D. The process parameters of Film A were chosen in a manner that a low plasma energy (200 W) a high silane (SiH_4) gas flow (320 sccm) and an additional ammonia (NH_3) gas flow (100 sccm) result in high residual concentration of nitrogen and hydrogen species and high tensile residual stress. The reason why such process conditions lead to high nitrogen and hydrogen impurities lead to can be explained by considering that the process parameters of Film C (production silane USG film) reveal the standard parameters for an almost stoichiometric USG film. Reducing the plasma power and adding an additional gas flow leads to a deposition process where not enough energy exists to excite the precursor gases properly. Therefore, hydrogen species coming from the incomplete decomposition of silane and ammonia species were implemented during the film growth. Nitrogen impurities are incorporated mainly due to additional ammonia gas flow.

The first evidence which supports this theory was the obtained refractive index results from the deposited USG films. Films B, C and D exhibited a refractive index of approximately 1.46 (at 670 nm) which is the reference value for stoichiometric silica glass (see Table 1). Film A had a refractive index of about 1.52. Higher relative concentrations of silicon and nitrogen species lead to an increasing refractive index, since the electronic structure in the dielectric material is different compared to SiO_2 . This can be seen in the refractive index of deposited silicon oxynitrides (SiO_xN_y) and stoichiometric silicon nitrides (Si_3N_4) [41]. Also the density of glasses has an impact

on the index of refraction, where a higher refractive index is obtained by the increase of the film density [42].

In terms of the measured stresses, Films B, C and D exhibited residual stresses in the compressive state. Such stresses can be seen as beneficial since ceramics and glass materials rely on residual compressive stresses to counteract harmful tensile stresses during application, tensile stresses often lead to material failure[18]. Film A had 72 MPa tensile film stress. When looking at the basic wafer curvature results of the four films (Figure 21), one can see that the stress-temperature behaviour between room temperature and 400°C in the heating segment is almost the same. This means that residual stresses arise by the chosen deposition parameters. In literature one can find correlations between residual stresses and used plasma power, whereby compressive stresses are usually obtained at higher RF-power [43]. This can be observed by comparing the RF powers of Film A and B. One fundamental physical explanation is the additional heat coming from the excited plasma species (ions, radicals, high energy electrons, etc.) [12]. This creates temperature differences between the deposition site and the bottom site of the silicon substrate which leads to thermal stresses in the material during deposition.

Since the silane gas flow is the rate limiting parameter for the chemical reaction $\text{Si}^* + 2\text{O}^* \rightarrow \text{SiO}_2$, Film A revealed a three times larger deposition rate than Film B. This also lead to the suggestion that the density of Film A is lower compared to the other three initial film systems. The high deposition speed could lead to voids or other small cavities and a higher incorporation of other gases. Evidence for a lower density of Film A after one thermal cycle was the obtained thermally resolved film thickness measurements. A higher refractive index and lower hardness values could be seen as further indications of a lower film density.

To be able to develop a qualitative material model for a USG film with nitrogen and hydrogen impurities, one has to also include the obtained chemical (FT-IR), mechanical (Nanoindentation) and film stress-temperature properties (wafer curvature). As stated in Section 1.7 three characteristic FT-IR vibrations represent a USG film. These vibration modes describe the nature between the bonding of silicon and oxygen, which leads to the structural properties shown in Section 1.3. Additional nitrogen and hydrogen change the chemical composition and the bonding characteristics. This leads to an FT-IR spectrum shown in Figure 16. N-H and H-N-H groups are incorporated into the glass network which led to a stretch vibration around

3400 cm^{-1} . Remaining hydrogen species were found due to incomplete oxidation of silane molecules leading to Si-H vibrations around 2200 cm^{-1} . Furthermore, a Si-N stretch band can be observed between 870-850 cm^{-1} strongly overlapped due to the incomplete oxidation of the SiO_2 structure which leads to band broadening and additional vibration modes caused by hydrogen species. Making the Si-O-Si bending vibration occurring around 800 cm^{-1} was hardly detectable. The improved silane based USG film, Film B and the two reference films, Film C (productive USG silane film) and Film D (productive USG TEOS film) only exhibited a small broad Silanol (Si-OH) band around 3600 cm^{-1} .

The mechanical properties showed that additional nitrogen and hydrogen incorporation in Film A lowered the elastic modulus and hardness. The extrapolated elastic modulus of Film A was about 10% lower than the other three films. The microscopic interpretation of the elastic modulus can be seen where the bonds between atoms yield in a spring system. The stiffness of each spring is determined by its specific bond energy function. Therefore, the elastic modulus depends on the nature of bonding and the amount of bonds present in the material. In Film A the chemical data suggest that due to the presence of high nitrogen and hydrogen concentrations incomplete condensation of SiO_4 tetrahedrons occurs and the lack of Si-O-Si bridging bonds lowers the Young's modulus.

With the obtained as-deposited results Figure 34 represents a two dimensional structure model of Film A. It can be seen that the glass network model of Film A exhibits an open structure which leads to cavities and open channels. Due to the additional nitrogen and hydrogen doping the network contains significant amounts of bonded nitrogen and hydrogen, which alter the glass chemistry of the USG film. As mentioned before, the origin of the impurities are generated by a non-balanced deposition process. To understand the as-deposited model of Film A it is necessary to recall the basic principles of covalent bonding.

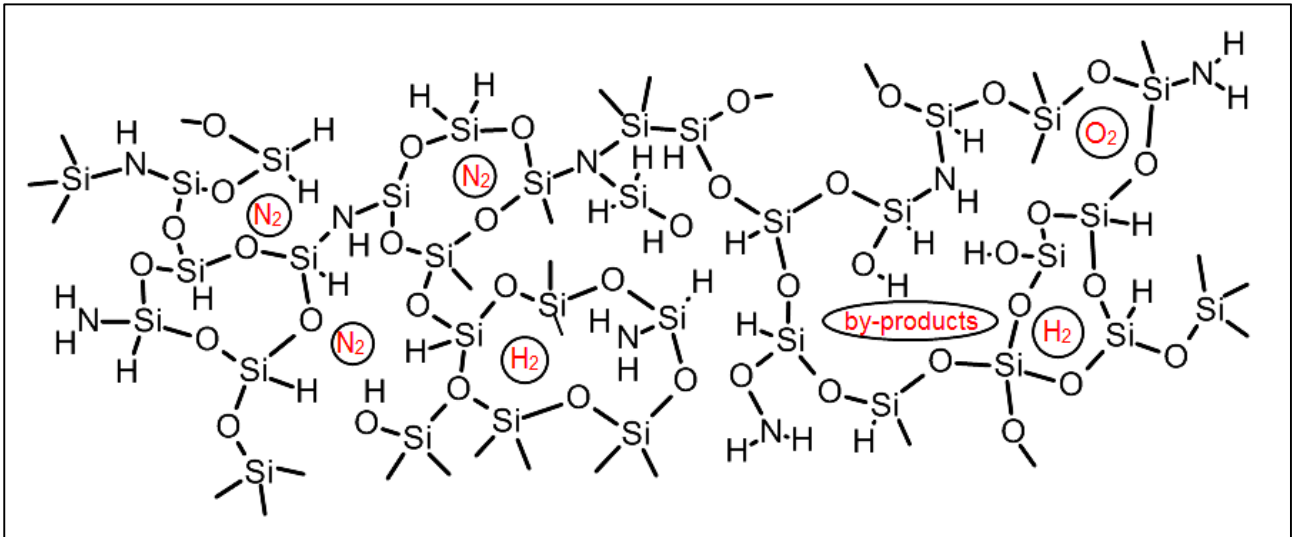


Figure 34: Structural 2-D model of Film A containing high nitrogen and hydrogen impurities after deposition.

Inorganic solids like glass exhibit a covalent bonding character. In covalent bonding the orbitals of the atoms overlap in order to share their valence electrons and form bonds. Therefore bonding and structural characteristics depend on the electronic properties of the involved atoms. In stoichiometric undoped silicon glass (USG) the silicon and oxygen atoms form SiO_4 tetrahedra which are connected via the oxygen atoms (=bridging atom). These two-fold coordinated O atoms are always connecting two tetrahedra. Hereby only Silicon, with the electronic valence configuration of $3s^23p^2$ (= four valence electrons) and oxygen, with a valence configuration of $2s^22p^4$ (= six valence electrons) form covalent bonds [44]. The hybridisation of the s and p orbital in silicon leads to four energetically equivalent sp^3 hybrid orbitals each sharing one electron pair with an oxygen atom (four sigma bonds). This directional bonding leads to the tetrahedral coordination of silicon which is shown in Section 1.3. The hybridisation of silicon and the resulting tetrahedral coordination is shown in Figure 35. The oxygen forms two directional σ bonds by overlapping its p-Orbital [45]. Since the O bridging atom is only two-fold coordinated a wide bond angle is the result, which is the main reason for the amorphous form SiO_2 [46], [47].

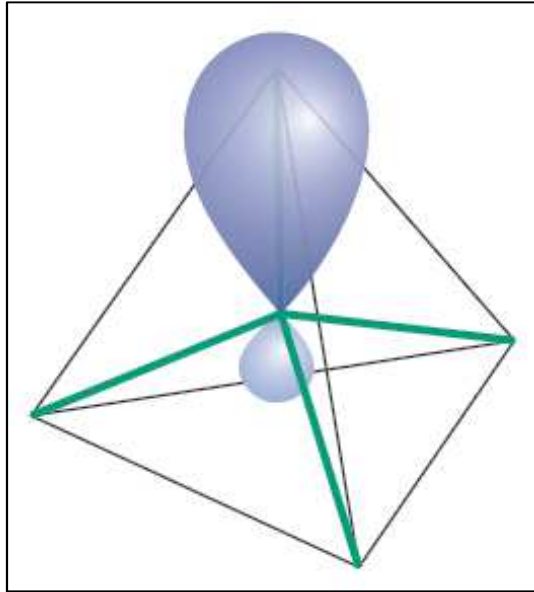


Figure 35: One of the four sp^3 hybrid orbitals of a silicon atom. Each one points towards a different vertex (green line) resulting in a regular tetrahedra [44].

The incorporation of nitrogen changes the USG chemistry in a fundamental way. Nitrogen has an electronic valence configuration of $2s^2p^3$ (= five valence electrons) which leads to the formation of three bonds instead of two. In pure amorphous silicon nitride (Si_3N_4) films Si-atoms are coordinated tetrahedrally to N-atoms like silicon in silicon dioxide, where sp^2 hybrid orbitals of nitrogen are overlapping with the three neighbouring silicon atoms with additional π bonding into the anti-bonding 3d orbitals of silicon. This forces the N-atom into a planar bonding arrangement with the three surrounding Si-atoms, which has been verified by Raman scattering in non-crystalline Si_3N_4 [48]. This implies a very strong bond in silicon nitride, which results in a very rigid structure and hence in an elastic modulus three times greater than in USG [49].

This leads to mixed bonding characteristics in Film A, caused by nitrogen doping. Hydrogen only forms weak single bonds since the first element of the periodic table possesses only one electron. The remaining hydrogen species bonded to Si and N-atoms results in a softer and less dense film which can be observed by looking at the observed mechanical and film thickness results in Sections 3 and 4.

The 2D structure model of the as deposited Film A (Figure 34) also suggests the incorporation of gas species (e.g.: N_2 , O_2 , H_2). The assumption is based on the fact that between $550^\circ C$ and $700^\circ C$ significant tensile stress generation in Film A can be observed (compared to an almost hydrogen and nitrogen free film, Film B), where thermally resolved FT-IR results show that the bonds cleave off the hydrogen atoms

at temperatures greater than 700°C. This is also supported by the high deposition rate of 21 nm/s compared to a three times lower rate in the deposition process of Film A. Incorporation of molecular species is also reported in literature [50].

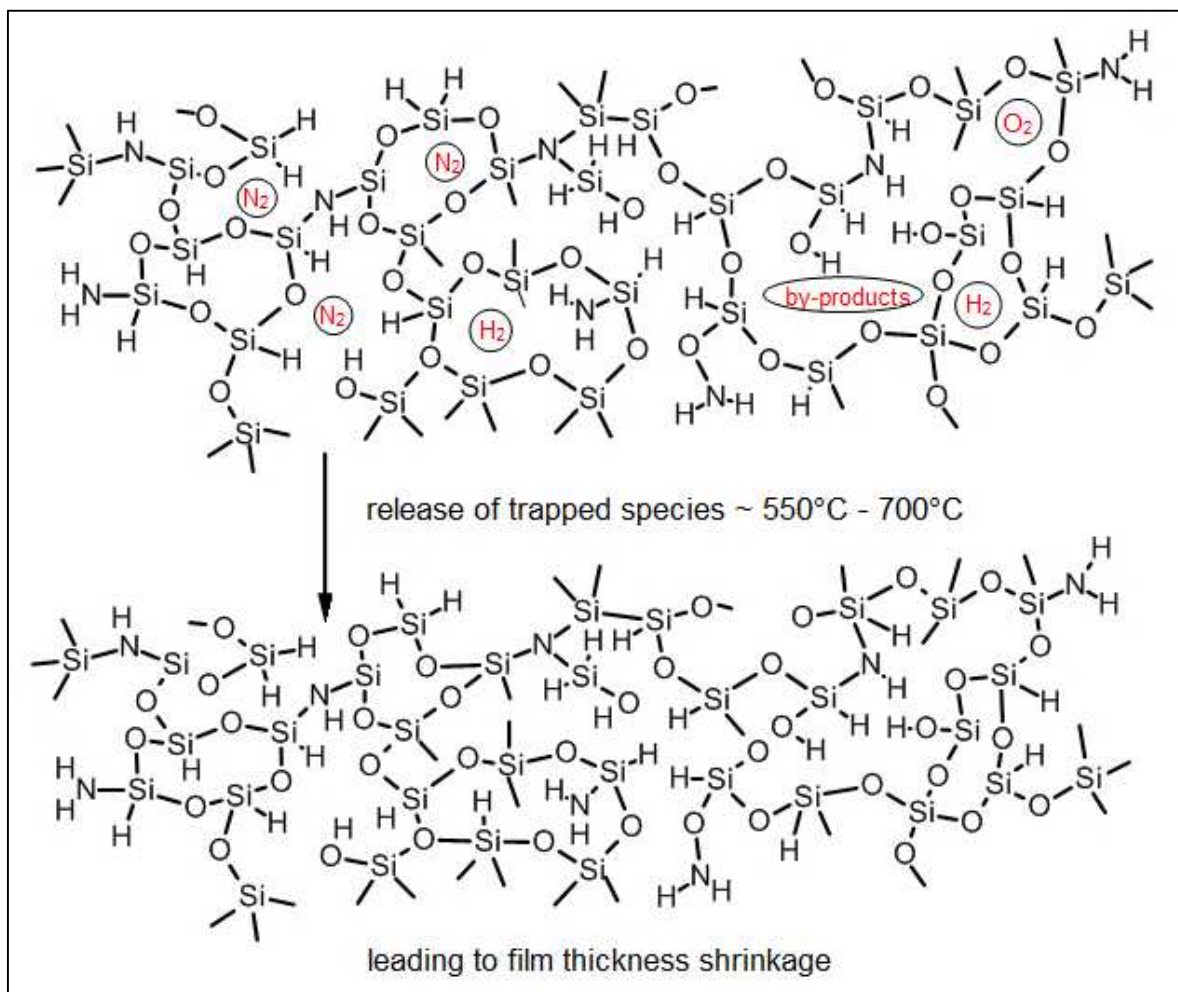


Figure 36: Film thickness shrinkage due to release of trapped molecular species in Film A.

The model suggests a spontaneous tensile stress generation caused by a thermally activated trap release process of incorporated molecular species. This process depends on the specific diffusion coefficient of the molecule and is temperature and size dependent. The temperature activated release of molecules leads to the densification of the glass network which can be observed in the thermally resolved film thickness data. Annealing studies have shown that the bond cleavage of hydrogen in Si-H and N-H species depends on the ratio of Si-H/N-H and the temperature of bond cleavage varies between 600 and 850°C with further cross linking reactions between the remaining nitrogen and silicon species [51]. The thermally resolved FT-IR data of Film A indicated that bond cleavage of hydrogen started around 700°C, with massive film thickness shrinkage and cracks obtained at peak temperatures of 800°C,

900°C and 1000°C (see Section 4). Similar film behaviour was observed in annealing studies of silicon oxynitride films [52].

Figure 36 shows the proposed hydrogen removal reactions and following cross linking reactions which lead to massive tensile stress generation and additional cracks in the film. The three hydrogen removal reactions should give possible cross linking reactions which are also reported in literature [51]. The driving force is the hydrogen bond cleavage and the formation of molecular hydrogen, since H-H has a higher bond energy compared to Si-H and N-H and promotes the formation of molecular hydrogen molecules [53]. This leads to additional film shrinkage due to further hydrogen species removal and the cross linking reactions described in Figure 37. In this illustration, reaction (a) displays the possible hydrogen formation via the bond cleavage between a neighbouring silanol (Si-OH) and a silane (Si-H) group. This leads to unpaired electrons in the remaining oxygen atom and silicon atom which leads to cross linking, and the creation of tensile stresses. The other two reactions follow the same principle where two silane groups (b) or one silane and an N-H group (c) lead to molecular hydrogen formation and additional cross linking. These three possible mechanisms only represent three most likely reactions which lead to hydrogen removal and crosslinking.

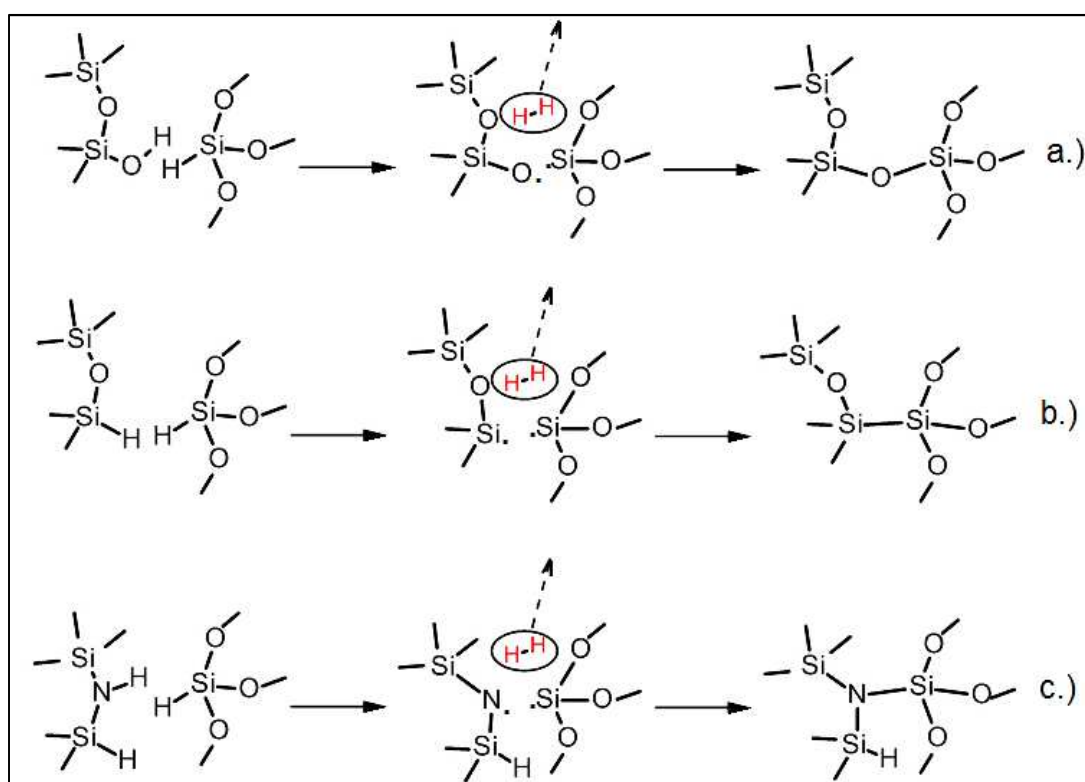


Figure 37: Three possible hydrogen removal reactions and following crosslinking between the remaining species. (a) reaction between a silane group (Si-H) and a Silanol group (Si-OH), (b) reaction between two Silane groups and (c) hydrogen removal via a Si-H and N-H group.

In literature various models exist where atomic hydrogen species are released leaving electronic defects back [45]. Such defects are indicated in the final structure figure where silicon and nitrogen atoms exhibit unpaired electrons. Since nitrogen and hydrogen exhibit different bonding characteristics to the silicon atom and the large decrease of hydrogen species forced the film to shrink, resulting in massive tensile stress generation. Figure 38 illustrates the structural situation of Film A after one thermal cycle. The exaggeratedly distorted bonds demonstrate that the film structure is under constraint due to the different bonding properties of nitrogen and hydrogen. This resulted in a massive stress built up at higher temperatures (700°C-1000°C) and as a consequence the film cracked. This resulted in a massive stress built up at higher temperatures (700°C-1000°C) and, as a consequence, the film cracked. The estimated tensile fracture stress was between 430 MPa and 780 MPa, since crack formation occurred between peak temperatures of 700°C and 800°C (see Section 4)

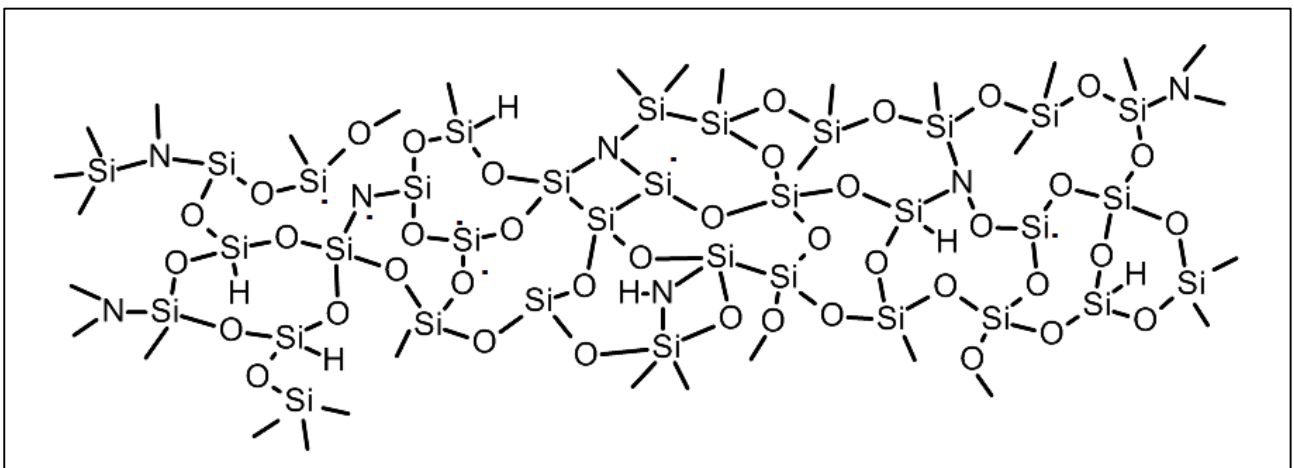


Figure 38: Structural model after heat treatment. The distorted structure indicates the generated tensile stresses due to hydrogen bond cleavage and following cross linking. The dots near silicon and nitrogen atoms indicate electronic defects in the glass network.

In terms of the separation of the nitrogen and hydrogen doping influence Film F (high H film) revealed almost the same stress temperature response with a few thin cracks. The wafer curvature data of Film F suggests a similar thickness-temperature as Film A as well, which would explain the cracks. In Film E the additional ammonia gas flow led to no cracks after one thermal cycle. The stress-temperature itself showed that up to temperatures of 700°C no additional stress evolution was observed (by comparing with the cooling segment around 700°C) and then showing additional stress build up which was followed by a stress plateau from around 860°C to 920°C. This would lead to the conclusion that remaining hydrogen removal (coming from introduced N-H species) and following crosslinking of nitrogen species in the silica glass network lead

to compressive stresses. A possible explanation could be the different planar hybridisation between nitrogen and its three silicon neighbours, which forced the network to stretch.

The high dopant concentration of nitrogen and hydrogen species had no influence on the surface topology, which can be seen on the unchanged roughness properties before and after heat treatment. The same observation was made for Films B, C and D suggesting that no surface diffusion was present, since the glass transition temperature is about 1200°C for stoichiometric USG [7].

Since the new wafer curvature device, which enabled stress-temperature measurements of semiconductor materials up to 1000°C, was the most important characterisation method of this project the capabilities and limitations of the method should be briefly discussed.

Wafer curvature results of Film A compared to Films B, C and D had shown enabled the observation of intrinsic stress evolution due to trap-release processes, hydrogen bond cleavage, the crosslinking of remaining unconnected species and the subsequent densification of the glass network. With the useful method of calculating the coefficient of thermal expansion by taking the lower part of cooling segment (300°C-150°C) where no thermally activated processes are present, Film A revealed a smaller CTE of about 1.9 ppm/°C, compared to the undoped USG films, Films B, C and D which showed a CTE of about 2.5 ppm/°C. A possible explanation would be the inverse relationship between the modulus of elasticity and the thermal expansion coefficient which is based on the bond energy function and, therefore, describes the nature of bonding and the resulting thermal and mechanical properties. Thereby materials with higher bond strength and resulting in a higher elastic modulus tend to have a lower coefficient of thermal expansion [54].

The thermally resolved film thickness measurements showed that after a complete thermocycle the thickness decreased about 11% of Film A. Especially in the peak temperature range from 700°C to 1000°C Film A lost about 7% of its film thickness. This demonstrates the limitations of the film stress measurement device. In the high temperature range the film thickness decreases and therefore the change of h_f is not negligible. In the software of the wafer curvature device, the film thickness has to be stated for the in-situ calculation of the film stress using the Stoney formula. It can be seen that the film stress has a linear dependence in terms of the film thickness. This implies that at higher temperatures (~600°C-1000°C) the film stress of Film A should

be higher than the displayed values. Since the film thickness changes in a dynamic manner, the upper part of the stress-temperature curve should reveal a higher stress increase. This would also explain the development of the loop like shape in the stress temperature curve of Film A. Furthermore, it has to be mentioned that the shape in the cooling part can be seen as correct since the since the relative stress change (with a constant film thickness) does not have any impact in the shape of the stress temperature curve and hence did not influenced the CTE measurements.

6. Summary and Future Work

In this project the influence of high residual concentration of nitrogen and hydrogen species in silane based USG films (Film A) was studied in terms of the properties from room temperature up to 1000°C. A wafer curvature instrument was used which enabled in-situ stress-temperature characterisations of the deposited amorphous glass films. The influence of hydrogen and nitrogen was studied in particular in terms of the crack behaviour and hence the change of the film properties caused by thermal treatment. The investigation of the highly doped silica glass film was performed in comparison with the two production USG films, Film C (silane based) and Film D (TEOS based) and the improved USG film, Film B. In the experimental section the films were tested in terms of their thermomechanical properties (wafer curvature), chemical properties (FT-IR), mechanical properties (elastic modulus and hardness via Nanoindentation), deposition properties (deposition stress, refractive index etc.) and surface properties (light microscopy, AFM). Furthermore, thermally resolved experiments on Film A were performed in order to get a deeper understanding of influence of the nitrogen and hydrogen species in USG films in thermal processes. The following statements should give a summary of the relevant results:

- Enablement of high temperature in-situ film stress measurement for semiconductor materials in inert atmospheres from room temperatures up to 1000°C (heating plate temperature) with a large range of heating and cooling rates.
- Deposition of silane based and TEOS based USG films, where Film A was doped with remaining nitrogen and hydrogen due to high silane flow and additional ammonia gas flow.
- Chemical analysis confirmed the presence of nitrogen and hydrogen species in Film A which led to the qualitative film composition of $\text{SiO}_x\text{N}_y\text{H}_z$ and SiO_xH_y for Films B, C and D.
- Massive intrinsic tensile stress evolution in Film A starting around 550°C which led to tensile stresses up to 1GPa due to hydrogen and nitrogen species in the glass network and irreversible stress changes after thermal cycling.
- Cracks in Film A were found after thermocycling as the result of the chemical changes and the subsequent densification of the film which led to

massive tensile stresses. Cracks formed between peak temperatures of 700°C and 800°C leading to tensile fracture stresses between 430 MPa and 780 MPa (see thermal resolved experiments).

- Increase of the elastic modulus in Film A from 59 to 96 GPa indicates the removal of hydrogen and the following cross linking reactions, while Films B, C and D revealed moduli which match with the bulk material fused silica (70 GPa)
- Removal of hydrogen species due to bond cleavage was observed at the temperature range from 700°C to 1000°C peak temperature using infrared spectroscopy for characterisation.
- The chemical analysis after the wafer curvature measurements suggests the composition of SiO_x ($x \sim 2$) for Films B, C and D and SiO_xN_y with almost no remaining hydrogen.
- Surface analysis showed that in all films no surface diffusion occurred since film roughness remained unchanged.
- Massive tensile stress generation can be assigned to hydrogen species (Film F) whereas higher amounts of nitrogen species led to a stress plateau around 900°C which implies a crosslinking due to nitrogen species in a compressive manner (Film E).
- Thermally resolved film thickness and refractive index measurements confirmed the densification of Film A. After one thermal cycle Film A lost about 11 % of its film thickness.
- The reduced film thickness also indicated the limitations of the wafer curvature method for amorphous glass films. The high chemical impurities led to film thickness shrinkage which gives altered film stress output, where error is scaled linearly by the film thickness
- Development of a qualitative structural two-dimensional model of the influence of nitrogen and hydrogen species in a thermal cycle. From room temperature up to around 500°C the structure reveals high amounts of nitrogen and hydrogen species and reactant molecules which are trapped in the glass network. From about 550°C to around 700°C intrinsic stress generation start due to trap release reactions and the begin of possible hydrogen bond cleavage. From about 700°C to 1000°C bond cleavage at Si-H and N-H species occurred which was followed by cross link reactions which led to further massive stress built up.

The statements above show the possibilities of the used characterisation techniques. The new wafer curvature measurement device showed the potential of in-situ stress temperature measurement at very high temperatures, which enabled the possibility to simulate thermal treatment processes which are used in semiconductor industry. Since the project was time limited, the new device still has more possibilities for the investigation of thermomechanical properties. The wide range of heating and cooling rates and the programmable temperature control enable the possibility of rate and time dependent thermocycles. For instance one can determine the viscoelastic properties of BPSG (boron phosphor silica glass) films since the glass transition temperature is in the used temperature range of the instrument [55]. Performing temperature depending experiments one has to think about temperature measurement and hence the importance of different thermal treatments. In this project the thermomechanical behaviour of USG films was investigated by heating a sample via a heating plate and subsequently measuring the film stress using the wafer curvature method. This is comparable to standard rapid thermal annealing process, where a wafer is heated on a ceramic heating plate. Other thermal processes are performed in quartz furnaces where the wafers are heated from outside via lamps. One can assume that the temperature distribution and the stress responses are completely different. The temperature itself is a very crucial topic in terms of the investigation of viscoelastic properties of an amorphous film. Therefore it is necessary to get information about the surface temperature of the sample during a thermal cycle. Since thermal conduction and hence the temperature of heated samples depends on many factors (surface roughness, thermal conductivity, absorption coefficient, emission coefficient) surface temperature calibrations using contact (thermal element) or non-contact (infrared pyrometer) techniques should be performed.

To develop a quantitative model of the influence of remaining nitrogen and hydrogen species in USG films additional measurement techniques would give information about the exact stoichiometry (Elastic Recoil Detection Analysis, Rutherford Back Scattering) [56]. The suggested future work should only show some possibilities of the high temperature measurement device for thin film investigation and additional characterisation methods, since the high number of semiconductor materials (crystalline or amorphous) and the different temperature intervals of interest.

Bibliography

1. *Handbook of Multilevel Metallization for Integrated Circuits*, ed. C.J.T. Syd R. Wilson, John L. Freeman 1993: Noyes Publications.
2. De los Santos, H.J., *Application of MEMS technology to RF/microwave systems*. 33rd European Microwave Conference, Vols 1-3, Conference Proceedings, 2003: p. 1439-1442.
3. Bishop, R.H., *Mechatronic Systems, Sensors, and Actuators: Fundamentals and Modeling*. 2 ed 2007: CRC Press.
4. Jain, J.R., et al., *A micromachining-based technology for enhancing germanium light emission via tensile strain*. *Nature Photonics*, 2012. **6**(6): p. 398-405.
5. Koh, K.H., Y. Qian, and C. Lee, *Design and characterization of a 3D MEMS VOA driven by hybrid electromagnetic and electrothermal actuation mechanisms*. *Journal of Micromechanics and Microengineering*, 2012. **22**(10).
6. Stratton, F.P., et al., *A MEMS-based quartz resonator technology for GHz applications*. *Proceedings of the 2004 IEEE International Frequency Control Symposium and Exposition*, 2005: p. 27-34.
7. Varshneya, A.K., *Fundamentals of Inorganic Glasses* 2006: Society of Glass Technology.
8. Brückner, R., *Properties and structure of vitreous silica. I*. *Journal of Non-Crystalline Solids*, 1970. **5**(2): p. 123-175.
9. Zachariasen, W.H., *The atomic arrangement in glass*. *Journal of the American Chemical Society*, 1932. **54**: p. 3841-3851.
10. Warren, B.E., *X-ray diffraction of vitreous silica*. *Zeitschrift Fur Kristallographie*, 1933. **86**(5/6): p. 349-358.
11. *Handbook of Deposition Technologies for Films and Coatings*, ed. R.F. Bunshah 1994: Noyes Publications.
12. Boogaard, A., *Plasma-enhanced Chemical Vapor Deposition of silicon dioxide: Optimizing dielectric films through plasma characterization*, 2011, University Twente.
13. Smith, D.L., *Thin Film Deposition: Principle and Practice* 1995, New York.
14. Landau, D.P. and S. Pal, *Monte Carlo simulation of simple models for thin film growth by MBE*. *Thin Solid Films*, 1996. **272**(2): p. 184-194.
15. Nix, W.D. and H.J. Gao, *An atomistic interpretation of interface stress*. *Scripta Materialia*, 1998. **39**(12): p. 1653-1661.
16. Doerner, M.F. and W.D. Nix, *Stresses and deformation processes in thin films on substrates*. *Critical Reviews in Solid State and Materials Sciences*, 1988. **14**(3): p. 225-268.
17. Gore, G., *On the properties of electrodeposited Antimony*. *Trans. Roy. Soc. (London)*, 1858. **158**.
18. Ohring, M., *Materials Science of Thin Films: Deposition and Structure* 2001: Academic Press.
19. Stoney, G.G., *The tension of metallic films deposited by electrolysis*. *Proceedings of the Royal Society of London Series a-Containing Papers of a Mathematical and Physical Character*, 1909. **82**(553): p. 172-175.
20. Chen, K.S. and K.S. Ou, *Modification of curvature-based thin-film residual stress measurement for MEMS applications*. *Journal of Micromechanics and Microengineering*, 2002. **12**(6): p. 917-924.
21. Chason, E., *Resolution and Sensitivity of Stress Measurements with the k-Space Multi-beam Optical Sensor (MOS) System*, 2005, Sandia National Laboratories.
22. Chason, E., *Use of kSA MOS System for Stress and Thickness Monitoring during CVD Growth*, 2000, Brown University.

23. Puigcorbé, J., A. Vilà, and J.R. Morante, *Thermal fatigue modeling of micromachined gas sensors*. Sensors and Actuators B: Chemical, 2003. **95**(1-3): p. 275-281.
24. Heinz, W., R. Pippan, and G. Dehm, *Investigation of the fatigue behavior of Al thin films with different microstructure*. Materials Science and Engineering a-Structural Materials Properties Microstructure and Processing, 2010. **527**(29-30): p. 7757-7763.
25. Smith, B.C., *Fundamentals of Fourier transform infrared spectroscopy* 2011: CRC press.
26. Lucovsky, G., et al., *Deposition of Silicon Dioxide and Silicon-Nitride by Remote Plasma Enhanced Chemical Vapor-Deposition*. Journal of Vacuum Science & Technology a-Vacuum Surfaces and Films, 1986. **4**(3): p. 681-688.
27. Lau, W.S., *Infrared Characterization for Microelectronics* 1999: World Scientific.
28. Fischer-Cripps, A.C., *Introduction to Nanoindentation* 2004: Springer Verlag.
29. Saha, R. and W.D. Nix, *Effects of the substrate on the determination of thin film mechanical properties by nanoindentation*. Acta Materialia, 2002. **50**(1): p. 23-38.
30. Cordill, M.J., *Adhesion of thin ductile films using stressed overlayers and nanoindentation*, 2003, Washington State University.
31. Meschede, D., *Optics, Light and Lasers* 2007: Wiley-VCH.
32. Ware, J.P.a.M., *Physics of Light and Optics* 2011c edition: available at optics.byu.edu.
33. De Garmo, E.P., J.T. Black, and R.A. Kohser, *DeGarmo's materials and processes in manufacturing* 2011: John Wiley & Sons.
34. Oliver, W.C. and G.M. Pharr, *Measurement of hardness and elastic modulus by instrumented indentation: Advances in understanding and refinements to methodology*. Journal of materials research, 2004. **19**(01): p. 3-20.
35. Bhushan, B. and X. Li, *Micromechanical and tribological characterization of doped single-crystal silicon and polysilicon films for microelectromechanical systems devices*. Journal of materials research, 1997. **12**(01): p. 54-63.
36. Okada, Y. and Y. Tokumaru, *Precise Determination of Lattice-Parameter and Thermal-Expansion Coefficient of Silicon between 300-K and 1500-K*. Journal of Applied Physics, 1984. **56**(2): p. 314-320.
37. Hughey, M.P. and R.F. Cook, *Massive stress changes in plasma-enhanced chemical vapor deposited silicon nitride films on thermal cycling*. Thin Solid Films, 2004. **460**(1-2): p. 7-16.
38. Moslehi, M.M., *Method and apparatus for real-time wafer temperature measurement using infrared pyrometry in advanced lamp-heated rapid thermal processors*, 1990, Google Patents.
39. Pert, E., et al., *Temperature measurements during microwave processing: the significance of thermocouple effects*. Journal of the American Ceramic Society, 2001. **84**(9): p. 1981-1986.
40. Sosman, R., *The properties of Silica*. Chemical Catalog Co., 1927.
41. Matoy, K., et al., *A comparative micro-cantilever study of the mechanical behavior of silicon based passivation films*. Thin Solid Films, 2009. **518**(1): p. 247-256.
42. Lucovsky, G., et al., *Low temperature growth of silicon dioxide films: A study of chemical bonding by ellipsometry and infrared spectroscopy*. Journal of Vacuum Science & Technology B: Microelectronics and Nanometer Structures, 1987. **5**(2): p. 530-537.
43. Tamulevicius, S., *Stress and strain in the vacuum deposited thin films*. Vacuum, 1998. **51**(2): p. 127-139.

44. Atkins, S., *Inorganic Chemistry* 2010: W. H. Freeman and Company.
45. Helms, C.R. and E.H. Poindexter, *The Silicon Silicon-Dioxide System - Its Microstructure and Imperfections*. Reports on Progress in Physics, 1994. **57**(8): p. 791-852.
46. Silva, J.R.G.D., et al., *Refinement of Structure of Vitreous Silica*. Philosophical Magazine, 1975. **31**(3): p. 713-717.
47. Mozzi, R.L. and B.E. Warren, *Structure of Vitreous Silica*. Journal of Applied Crystallography, 1969. **2**: p. 164-175.
48. F. L. Galeener, W.S., and G. T. McKinley, in *The Physics of MOS Insulators*. (Pergamon, New York), 1980: p. p.77.
49. Taylor, J.A., *The Mechanical-Properties and Microstructure of Plasma Enhanced Chemical Vapor-Deposited Silicon-Nitride Thin-Films*. Journal of Vacuum Science & Technology a-Vacuum Surfaces and Films, 1991. **9**(4): p. 2464-2468.
50. Mani, S. and T. Saif, *Stress development in plasma-deposited silicon dioxide thin-films due to hydrogen evolution*. Thin Solid Films, 2007. **515**(5): p. 3120-3125.
51. Habraken, F.H.P.M., *LPCVD Silicon Nitride and Silicon Oxynitride Films (EU research project)* 1991: Springer Verlag.
52. Denisse, C.M.M., et al., *Annealing of plasma silicon oxynitride films*. Journal of Applied Physics, 1986. **60**(7): p. 2543-2547.
53. Lucovsky, G., Z. Jing, and D.R. Lee, *Defect properties of Si-, O-, N-, and H-atoms at Si-SiO₂ interfaces*. Journal of Vacuum Science & Technology B, 1996. **14**(4): p. 2832-2839.
54. Barker, R.E., *An Approximate Relation Between Elastic Moduli and Thermal Expansivities*. Journal of Applied Physics, 1963. **34**(1): p. 107-116.
55. Van Cleemput, P.A., *In-Situ Flowing BPSG Gap Fill Process Using HDP*, 1999, Google Patents.
56. Amaratunga, G. and S.R.P. Silva, *Nitrogen containing hydrogenated amorphous carbon for thin film field emission cathodes*. Applied Physics Letters, 1996. **68**(18): p. 2529-2531.